International Journal of Heat and Mass Transfer 241 (2025) 126711

Contents lists available at ScienceDirect

International Journal of Heat and Mass Transfer

journal homepage: www.elsevier.com/locate/hmt

Analytic thermal conductance for square channel, flat plate oscillating heat pipe: CFD simulations of Taylor liquid film and experiment

Fan Lu [a], Lorenzo Franceschetti [a], Kyle Krippner [a], Massoud Kaviany [a,*], Takuro Daimaru [b]

[a] Department of Mechanical Engineering, University of Michigan, Ann Arbor, MI, 48109, United States
[b] Two-Phase Technology, NASA Jet Propulsion Laboratory, Pasadena, CA, 91101, United States

ARTICLE INFO

Keywords:
Square microchannel
Oscillating heat pipe (OHP)
Thermal conductance (thermal resistance)
Numerical simulation (CFD)
Slug and plug

ABSTRACT

In oscillating (pulsating) heat pipes (OHP, PHP), square channels offer fabrication simplicity (e.g., 3-D printing) and have shown improved thermal performance over circular channels. It has also been suggested that the peripheral averaged slug-deposited liquid film thickness for square and circular cross sections are similar, though the presence of the corners alters the fluid dynamics significantly. Here, using isothermal CFD, the axial development of the Taylor liquid film behind a passing liquid slug in the square capillary channel is predicted. The results show that the film thickness varies peripherally and axially. The heat transfer in the evaporator is simulated by non-isothermal CFD and is dominated by liquid film evaporation. This liquid film conductance is inversely proportional to the peripheral-varying thickness. An analytic, upper-bound OHP thermal conductance is proposed based on an effective liquid film thickness, $G_{\delta_l} = \frac{k_l}{\delta_{l,sc,c}}\left(\frac{1}{A_e}+\frac{1}{A_c}\right)^{-1}$. In a companion experiment, a 3-D-printed square-channel (side dimension of 1 mm) flat-plate OHP (FPOHP) using R-134a as the fluid is tested, and the measured conductance is compared with the predicted upper bound. In FPOHP, the heat conduction between adjacent channels negatively affects the conductance; however, this effect is compensated by enhanced internal conductance. An existing 1-D heat-mass-momentum conserved simulation is extended to the square channel geometry and used to assess this 3-D plate conduction. A reasonable agreement (up to 80 percent) was found between the experiments and the simple, analytic upper-bound OHP thermal conductance.

1. Introduction

In recent years, Additive Manufacturing, such as laser, metallic powder-bed fusion, of the flat plate oscillating heat pipe (FPOHP) has shown ease of fabrication and good thermal performance, especially using a channel of square cross-section [1,2]. The square cross-section channels have shown larger conductance at high heat load, compared to circular channels, and with the opposite trend at low heat load [1]. In addition, the sintered powder surfaces of the FPOHP channels have capillary roughness and crevices that can assist with the surface liquid coverage [2]. However, if the thermal conductivity of the solid material is large, this can impact the overall thermal conductance of the FPOHP. As analyzed using numerical simulations and experiments, [3] determined that the thermal interaction among adjacent FPOHP channels reduces the overall FPOHP conductance. This effect is attributed to an equilibrium in temperature and pressure between channels, which reduces the non-equilibrium-based oscillatory motion corresponding to effective OHP performance, which is also discussed in [4]. Thus, the larger conductance of the square channel geometry is partially offset by embedding it within a larger solid (such as by additive manufacturing techniques).

The moving-slug-deposited liquid film is important in oscillating (pulsating) heat pipes (OHP), as it is related to the overall heat transfer and performance characteristics. The fluid mechanics of this liquid film has been studied through CFD simulations [5,6] and experiments [7]. Among the particular features of this liquid film is the persistence of the contact line location (referred to as the pinning location), and a continuous increase in the peripheral-averaged film thickness with the axial location in the transition region. Figs. 1(a) (right channel) and (b) demonstrate these features. Figs. 1(a) to (d) show the two-phase fluid flowing through a U-turn, with liquid film formed by moving single slugs with a contact line or by two moving slugs. Liquid films with the contact line locations (pinning locations) are common in OHP, where they are often observed in between a dry region (at the left of the pinning location) and a liquid slug region (at the right of the bubble head) in both experiments with transparent channels [3,8], and in 1-D OHP simulations [9]. The Taylor bubble film is formed around a moving gas bubble (plug) in between two liquid slugs. The Taylor bubble film is

* Corresponding author.
E-mail address: kaviany@umich.edu (M. Kaviany).

https://doi.org/10.1016/j.ijheatmasstransfer.2025.126711
Received 6 November 2024; Received in revised form 8 January 2025; Accepted 9 January 2025

Nomenclature

Roman Symbols

A	area, m^2
a	modification factor
Bo_D	Bond number, $\frac{(\rho_l-\rho_g)gD^2}{\sigma}$
Ca_D	Capillary number, $\frac{\mu_l u_l}{\sigma}$
D	hydraulic diameter, m
$\boldsymbol{f}$	volumetric body force vector, N/m^3
Fr_D	Froude number, $\left[\frac{\rho_l u_l^2}{g(\rho_l-\rho_g)D}\right]$
G	thermal conductance, W/K
Δh_{lg}	heat of evaporation, J/kg
h	heat transfer coefficient, W/m^2-K; specific enthalpy, J/kg
k	thermal conductivity, W/m-K
La_D	Laplace number, $\frac{\sigma\rho_l D}{\mu_l^2}$
L, l	length, m
$\dot{M}$	mass flow rate, kg/s
$\dot{m}$	mass flux, kg/m^2-s
M	mass, kg
$\dot{n}$	volumetric mass generation, kg/m^3-s
N	number of turns
P	channel perimeter, m
p	pressure, Pa
T	temperature, K
$\boldsymbol{q}$	heat flux vector, W/m^2
Q	heat load, W
Re_D	Reynolds number, $\frac{\rho_l u_l D}{\mu_l}$
R	thermal resistance, K/W; radius, m
$\boldsymbol{s}_n$	surface normal vector
$\boldsymbol{u}$	velocity vector, m/s
We_D	Weber number, $\frac{\rho_l u_l^2 D}{\sigma}$

Greek Symbols

α_l'	modified filling ratio
α_i	phase$i$ volume fraction
δ_l	liquid film thickness, m
μ	dynamic viscosity, Paλs
ν	kinematic viscosity, $m^{2/s}$
ρ	density, kg/m^3
σ	surface tension, N/m
θ_c	contact angle, °

Subscripts

c	constant
cnr	channel corner
ctr	channel center
d	dryout
e	evaporator
h	hydraulic, averaged-inverse
i	inlet, phase
l	liquid
lg	liquid–gas (vapor) phase change
n	normal
o	outlet
s	slug, solid
sc	square channel
t	tangential
u	convective
w	wall
xy	peripheral plane
z	axial coordinate

Superscript

*	dimensionless

Others

$\langle\ \rangle$	spatial average

similar to the slug-deposited film but does not include the contact line as shown in Figs. 1(a) (left channel) and (d). The average film thickness variation with the slug velocity in the uniform-film region is observed to have a similar trend as the existing film thickness correlation for the circular cross-section in [10], which is supported by simulations reported in [11] using free-surface-Stokes flow equations. While the liquid film in a capillary, circular cross-section channel has peripheral (angular) uniformity, the square cross-section creates a non-uniform peripheral film thickness. The channel corners have the largest film thickness $\delta_{l,\mathrm{cnr}}$, while the thinnest film thickness occurs between the corners [10,12,13], as shown in Fig. 1(c). The film deposited by a long moving plug shows a parabolic distribution near the channel center observed with a chromatic interference method [14]. Transversal flows may cause the non-uniformity of peripheral deposited films, also called draining flows, which move the liquid from the channel centers to the corners [15]. This phenomenon is not observed in the circular channels. The Taylor liquid-film fluid dynamics in circular microchannels has been previously simulated using ANSYS Fluent [16]. The dynamics of the deposited film are important since they control the local heat transfer coefficient based on liquid-film conduction [17]. Depinning occurs once the liquid film reaches a critical length, and the corner roundness can affect the critical length [7].

There are three regions in the flow-boiling microchannels: (i) a liquid slug, (ii) an evaporating elongated bubble, and (iii) a dry-out region [17]. In a thorough numerical analysis of the Taylor bubble liquid film in square microchannels under evaporation [15], the liquid film thickness varies peripherally, resulting in exceptionally large heat transfer in the channel center regions, while the heat transfer through the corners is rather small. The authors showed that liquid convection increases the local heat transfer coefficient depending on the axial location. The previously mentioned study is for a Taylor-type bubble flow, while the thermal performance of the slug-deposited film remains undefined. The heat transfer coefficient of refrigerant R-134a flowing inside a circular microchannel has also been measured under a constant injection rate [18–20]. The vapor (gas) flow has significant turbulence and vortical behavior at low Reynolds numbers [21,22]. In addition, it has been shown that the discretization of the near-wall mesh can significantly impact the simulation performance [23]. For accurate modeling, these behaviors need to be addressed using CFD turbulence models of transitional regions.

The overall thermal conductance, G, is a measure of the heat transfer performance of OHP. Thin liquid film conduction and liquid–vapor interfacial evaporation have been identified as the dominant mechanisms controlling this overall thermal conductance (or resistance R) [24–26]. In addition, heat transfer occurs through liquid (film and slug) convection [26]. Using CFD simulations with prescribed liquid slug length and vapor inlet conditions and operational conditions such

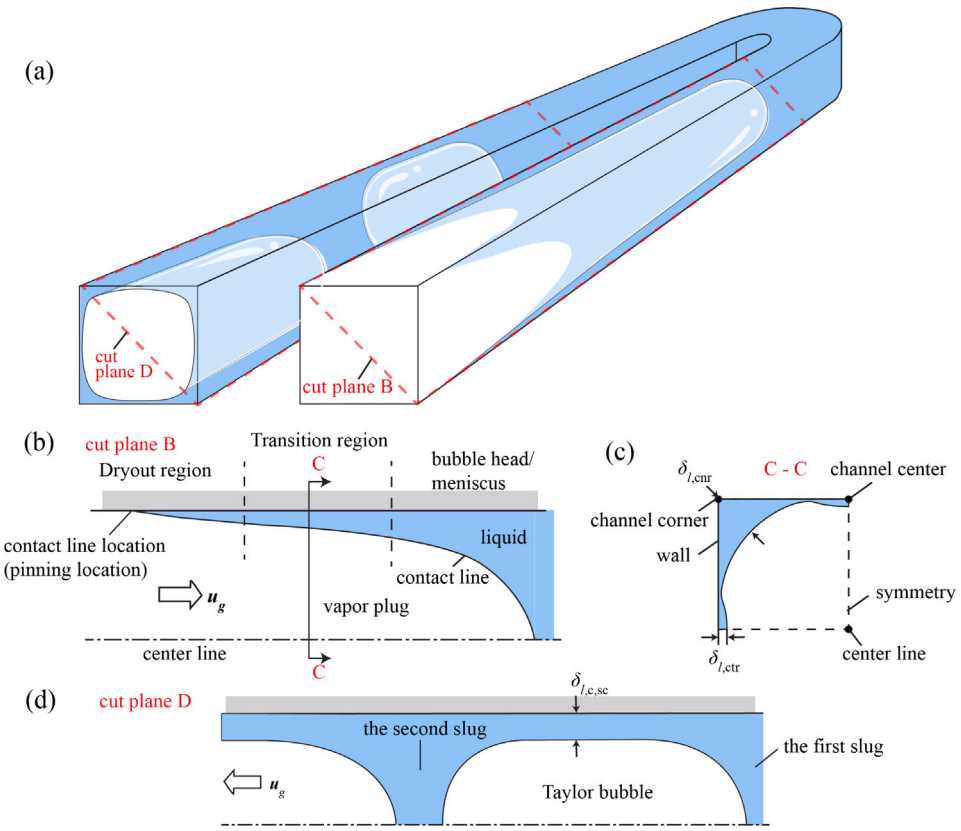

Fig. 1. (a) A schematic of two-phase flow in a square capillary channel and through a bend, showing liquid formed behind a single slug with the contact line, and liquid film formed between two moving slugs. (b) Axial, and (c) peripheral liquid distributions, for the moving-slug-deposited film. The passing slug is to the right, and the vapor plug behind is also shown. A quadrant of the cross-section is shown with the assumed symmetries. (d) The liquid film formed between two moving slugs in the diagonal axial plane.

as the surface heat flux and slug velocity [27], allows for predicting an upper limit on the overall thermal conductance G at the high heat load limit, and this has been verified for a circular cross-section OHP [28]. Recently, there has been a comparison of OHP with single and double-condenser (on both ends), and the results show that the double condenser has a higher thermal conductance and a more stable operation with a wider range of temperatures and filling ratios [29], but the distance between the evaporator and the condensers is also cut in half.

Here we study the fluid mechanics and heat transfer characteristics of an evaporating, deposited liquid film in a square microchannel. Using isothermal CFD simulations with different inlet plug velocities, we examine the fluid mechanics of the deposited film, including the axial and peripheral film thickness distribution and liquid flow. Non-isothermal simulations are also performed under evaporation to determine the liquid film heat transfer characteristics in the three axial regions. The fluid is saturated refrigerant R-134a at 300 K (7 atm pressure) flowing in a square channel with a side dimension W of 1 mm. The refrigerant has a thermal conductivity k_l of 0.10 W/m-K, and surface tension coefficient σ, specific heat c_p, and dynamic viscosity μ_l are about 0.007 N/m, 1.43 kJ/kg-K, and 0.00021 Pa-s, respectively. A simple and analytic circular OHP conductance model is used as an upper limit on the overall thermal conductance in [28]. A similar model is adopted to square cross-section OHP in this study. This ideal conductance model is based on complete coverage of the channels with the thin liquid film. Since the film thickness is peripherally non-uniform for a square channel, we introduce modification coefficients to the model to account for this, based on CFD results. In a related experiment, an additively manufactured FPOHP operating with R-134a is tested, and the measured conductance is compared with the predicted ideal conductance. Finally, 1-D heat-mass-momentum (1-D HMM) OHP simulations [9] are also used in this study to validate the results, and to extract the important effect of 3-D solid conduction when the square channels are embedded in a flat-plate solid structure (FPOHP).

2. Slug-deposited liquid film simulations

The 3-D numerical simulations of two-phase slug flow are performed. The length of the isothermal simulation domain is 25 mm, while a length of 12.5 mm was used for non-isothermal cases due to the required mesh size and the limit of computational resources. We compare the results for the isothermal and non-isothermal simulations for when the meniscus front reaches the same distance from the entrance. So, the total pipe length does not influence the results (although the isothermal simulation length is twice the length of the non-isothermal simulation). An example is in Supplementary Materials Figure A.4, where the axial variation of peripheral average liquid film thickness for both isothermal and non-isothermal simulations are shown. The longer isothermal simulation domain gives more results about the axial development of the meniscus, where the liquid film thickness distributions for different velocities intersect at $z = 14$ mm. A shorter domain is used for non-isothermal cases because of the required finer mesh size (a lot more computationally intensive). More details about the simulation conditions including coordinates, initial conditions, geometrical parameters, and boundary conditions are shown in Fig. 2. The hydraulic diameter of the isothermal simulations is 0.8 mm which matches the diameter used in [28]. The hydraulic diameter for the non-isothermal simulation, 1-D HMM simulation, and experiment is 1 mm. The fully-developed vapor inlet velocity distribution in a square channel follows [30]

$$u_{g,i}(x,y) = \frac{\langle u_g \rangle}{\pi}\left(1 - \frac{\cosh(\pi y/2D)}{\cosh(\pi/2)}\right)\cos(\pi x/2D), \quad (1)$$

where $\langle u_g \rangle$ is the mean velocity of the inlet gas plug, and D is the hydraulic diameter. The constant surface (wall) heat flux is chosen as

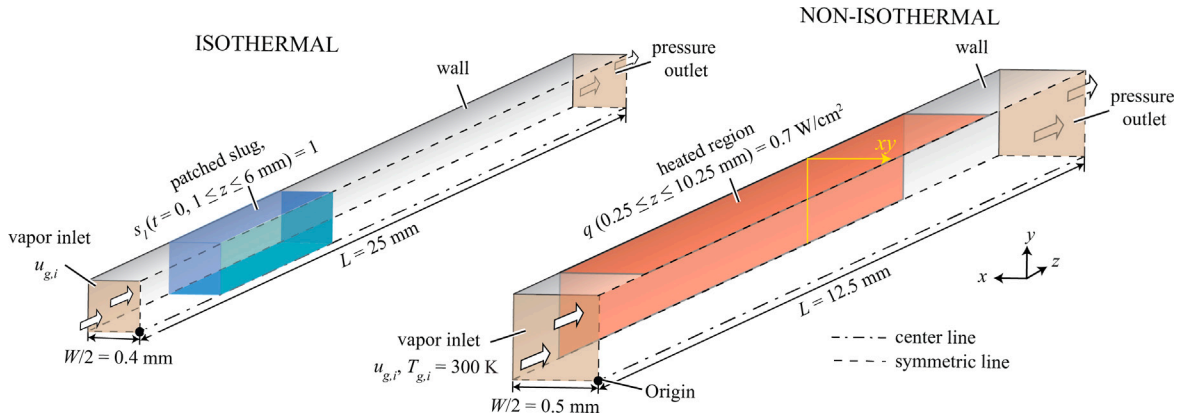

Fig. 2. Schematics of the isothermal and non-isothermal simulation conditions of slug liquid-film deposition. The liquid slug is patched in the isothermal domain as an initial condition. The non-isothermal axial length is shortened for computational economy.

it represents the flat-plate (embedded) OHP heat input and allows for using the simple relation between the vapor inlet velocity and constant heat flux Eq. (32) developed in [28]. Due to the symmetries of the square channel (no gravity effect in capillary channels), the simulation domain is a quadrant with two symmetry planes (the dashed lines in Fig. 2).

2.1. Numerical method

The ANSYS Fluent (release 2022 R2) code was used to solve the two-phase fluid mechanics and energy equations treated with the Eulerian method coupled with a Multi-Fluid VOF model, which allows each phase to have its own velocity, while still allowing for a sharp interface between phases. In our simulations, since the Reynolds number spans from laminar to turbulent-flow regime, we used the baseline (BSL) k-ω viscous model combined with an algebraic intermittency model to account for laminar-to-turbulent transition. This Reynolds-Averaged Navier–Stokes (RANS) two-equation model employs the Boussinesq approximation, inspired by molecular diffusion, to calculate eddy viscosity. The algebraic intermittency model can handle viscosity-dominated flow near the wall. Although no calibrated laminar-to-turbulent transition model exists for fully developed pipe flow, tests have shown that this simplified transition model was suitable for our simulation. The k-ω model was chosen over the k-ε model due to its superior ability to capture near-wall behavior in slug flow. These analyses and more details about the performances of different models are also included in [28].

Similar to [28], incompressible fluid flow is assumed for both liquid and vapor phases along with constant thermophysical properties (temperature variations within the operating range considered vary less than 10°C). The saturation temperature is assumed constant since the pressure change in the simulation is negligible. The viscous dissipation and gravity effects are assumed negligible (large Froude number). The vapor temperature is set to the saturation temperature (the vapor cannot be superheated)

$$T_g = T_{lg}, \tag{2}$$

where g stands for gas (vapor, since a single-component fluid is assumed), and lg for liquid–gas saturation The local phase volume fraction of the liquid and vapor (gas) phases are α_l and α_g, which are constrained by,

$$\alpha_l + \alpha_g = 1, \tag{3}$$

where subscript l stands for liquid. The continuity and momentum conservation equations for each phase are ($i = l$ or g, then j is the other phase)

$$\frac{\partial}{\partial t}(\alpha_i \rho_i) + \nabla \cdot (\alpha_i \rho_i \boldsymbol{u}_i) = -\dot{n}_{ij} \tag{4}$$

$$\frac{\partial}{\partial t}(\alpha_i \rho_i \boldsymbol{u}_i) + \nabla \cdot (\alpha_i \rho_i \boldsymbol{u}_i \boldsymbol{u}_i) = -\alpha_i \nabla p + \nabla \cdot [\mu_i (\nabla \boldsymbol{u}_i + \nabla \boldsymbol{u}_i^T)] - \dot{n}_{ij} \boldsymbol{u}_{ij} + \boldsymbol{f}, \tag{5}$$

where p and μ_i are the pressure and viscosity of phase i. $\dot{n}_{ij}$ (kg/m^3-s) is the volumetric phase change rate. $\boldsymbol{f}$ is the volumetric force vector exerted on the interface. The energy equation for each phase is

$$\frac{\partial}{\partial t}(\alpha_i \rho_i h_i) + \nabla \cdot (\alpha_i \rho_i \boldsymbol{u}_i h_i) = \alpha_i \frac{\partial p_i}{\partial t} - \nabla \cdot \boldsymbol{q}_{k,i} - \dot{n}_{ij} \Delta h_{ij} - Q_{ij}, \tag{6}$$

where h is the specific enthalpy, $\boldsymbol{q}_k$ is the conductive heat flux, Δh_{ij} is the latent heat, and Q_{ij} is the heat transfer rate from phase i to j.

2.1.1. Surface tension and wall adhesion forming liquid film

In an oscillating heat pipe, the working fluid exists as liquid slugs separated by vapor plugs with curved menisci. The surface tension (along the interface) helps stabilize the meniscus and is caused by attractive forces among fluid molecules. Specifically, the surface tension tends to minimize surface free energy by decreasing the area of the interface. The continuum surface force (CSF) model proposed in [31] interprets surface tension as a continuous three-dimensional effect across an interface, instead of a boundary condition on the interface. These surface tension effects are modeled by adding a source term in the momentum equation. The interfacial pressure drop is related to the surface tension coefficient σ, and the surface curvature is measured by two principal radii, R_1 and R_2 of meniscus curvature, which is known as the Young–Laplace equation:

$$p_i - p_j = \sigma(1/R_1 + 1/R_2). \tag{7}$$

Eq. (7) defines the pressure drop across the interface. The sum of the inverses of two principal radii is defined as the curvature, which is κ. This equation serves to determine the surface tension force $\boldsymbol{f}$, which is an essential part of the multiphase Navier–Stokes equations, i.e., Eqs. (4), (5). The liquid film thickness can then be determined by solving the Navier–Stokes equations with the finite volume method. The surface tension coefficient is assumed constant in this study due to the relatively small change in the temperature in the non-isothermal simulations. So, there should not be an observable change of surface tension due to temperature.

The interface surface normal vector $\boldsymbol{s}_n$ is defined as the gradient of the volume fraction of phase i, α_i, i.e.,

$$\boldsymbol{s}_n = \nabla \alpha_i, \tag{8}$$

and the curvature κ is

$$\kappa = 1/R_1 + 1/R_2 = \nabla \cdot \frac{\boldsymbol{s}_n}{|\boldsymbol{s}_n|}. \tag{9}$$

For two-phase flow we have

$$\kappa_i = -\kappa_j, \nabla \alpha_i = -\nabla \alpha_j. \tag{10}$$

Table 1
Dimensionless numbers for each isothermal simulation velocity case in CFD, for working fluid R-134a and hydraulic diameter $D = 0.8$ mm.

u_l, m/s	$\mathrm{Re}_{D,l}$	Ca_D	We_D	La_D	Bo_D	Fr_D	μ_l/μ_g	ρ_l/ρ_g
0.2	919	0.00522	4.8			2.3		
0.3	1379	0.00783	10.8			3.4		
0.4	1838	0.0104	19.2	1.8	0.91	4.6	17	35
0.5	2298	0.0130	30.0			5.7		
0.75	3447	0.0196	67.4			8.6		

The surface tension can be expressed as a volumetric force using the divergence theorem. This volumetric force term in the Eq. (5) becomes

$$\boldsymbol{f} = \sigma \frac{(\alpha_i \rho_i + \alpha_j \rho_j)\kappa_i \nabla \alpha_i}{1/2(\rho_i + \rho_j)}. \tag{11}$$

The curvature of the interface near the wall is related to the contact angle, which is expressed as

$$\boldsymbol{s}_n = \boldsymbol{s}_{n,w}\cos\theta_c + \boldsymbol{s}_{t,w}\sin\theta_c, \tag{12}$$

where $\boldsymbol{s}_{n,w}$ and $\boldsymbol{s}_{t,w}$ are the unit vectors normal and tangential to the wall, respectively, and θ_c is the contact angle.

2.2. Two-phase flow dimensionless numbers

Several dimensionless numbers are used to characterize the fluid mechanics of the two-phase flow and film deposition in the square channel OHP. Some dimensionless numbers can be used as independent variables when comparing the film conductance of different types of fluid. The liquid inertia and viscous effects (in the liquid slug) are related through the Reynolds number. The capillary number describes liquid–vapor interfaces using the ratio of viscous forces to the surface tension of the fluid. Similarly, the Weber number relates the inertia of the liquid phase to the surface tension, and this is relevant to the liquid film deposition. The Laplace number is used to relate surface tension to the viscous forces. The Bond and Froude numbers are both used to characterize the importance of gravitational force in the system, describing its relationship with surface tension and fluid inertia, respectively. The Mach number $\mathrm{Ma} \ll 0.3$, so gas compressibility is not important. The expressions for these relevant dimensionless numbers are defined as

$$\begin{aligned} &\mathrm{Re}_D = \frac{\rho_l u_l D}{\mu_l}, \mathrm{Ca}_D = \frac{\mu_l u_l}{\sigma}, \mathrm{We}_D = \frac{\rho_l u_l^2 D}{\sigma} \\ &\mathrm{La}_D = \frac{\sigma \rho_l D}{\mu_l^2}, \mathrm{Bo}_D = \frac{(\rho_l - \rho_g) g D^2}{\sigma}, \mathrm{Fr}_D = \left[\frac{\rho_l u_l^2}{g(\rho_l - \rho_g) D}\right]. \end{aligned} \tag{13}$$

The ranges of these dimensionless numbers with five different velocities are presented in Table 1, some of which are used in the isothermal CFD simulations.

3. Isothermal slug-deposited liquid film CFD results

Isothermal simulations of a moving slug depositing a liquid film on a square-channel wall are implemented to observe the liquid motion and the film thickness distribution in the peripheral and axial planes. The validation of the CFD results is presented in Supplementary Materials B. The boundary conditions, initial conditions, and geometries are shown in Fig. 2. The initially stationary slug is pushed by the entering gas the in axial direction ($+z$) with a non-uniform velocity distribution of Eq. (1). Fig. 3(a) shows the distribution of liquid volume of fraction in the oblique plane (cutting through the channel corner, δ_{cnr}). In the upstream of the slug, some small dry patches appear near the channel center, as shown in Fig. 3(b). This phenomenon has also been reported in [7], and is caused by the liquid film depinning. The depinning occurs when the films grow in length as the vapor plug advances downstream and reaches a critical length [7]. The surface tension forces are no longer able to sustain the film attachment, leading to depinning.

3.1. Peripheral and axial liquid flows

As the vapor plug moves downstream, liquid movement creates a thick film at the channel corner. Eq. (11) describes the equivalent volumetric force $\boldsymbol{f}$ applied by surface tension. The surface tension force points towards the gradient of liquid volume fraction α_l. As shown in Fig. 4(a) at the liquid–vapor interface, there are x and y components of the surface tension, with the x component pressing the liquid against the wall, while the y component shears the liquid surface upward. The surface tension minimizing the surface free energy tends to decrease the interfacial area, forcing the liquid toward the corner. The pressure distribution in the liquid and gas phases and its corresponding liquid volume fraction are shown in Fig. 4(b). In Eq. (5), the surface tension force is a source term that acts as a pressure jump across the interface, given by Eq. (11), and is a function of the curvature. At the channel center, as shown in Fig. 4(a), the curvature is not as large as it is in the channel corner. Thus, the local liquid pressure is lower in the corners. In some locations, the curvature at the corner is negative, i.e., the interface curves towards the vapor phase, as shown in Fig. 1(c). The local pressure is even larger than the vapor pressure, which is not as obvious in Fig. 4(b). Similar results have been reported in [15], simulating the Taylor bubble film in a square channel passing through an adiabatic and then a heated region. Fig. 4 is a snapshot of an animation (video) which can be found in Supplementary Material B.

Fig. 5 presents the pressure and liquid velocity vector field distributions in the diagonal (oblique) plane cutting through the channel corner and showing the longitudinal meniscus topology. The axial pressure gradient in the slug region is larger than the film and vapor phase. The pressure jump across the liquid–vapor interface is obvious and it depends on the curvature. The bubble-head has the largest pressure jump since its curvature is large in both peripheral and axial planes. In the transition region, the curvature of the interface is large in the peripheral plane but not in the axial plane. In the velocity vector field, the maximum velocity is at the center line of the channel, which is about 0.75 m/s, compared to the mean of 0.5 m/s. The velocity in the film is about 0.1 m/s. Starting from the bubble head, the deposited film thickness decreases until the pinning location is reached, where the film thickness is zero. This differs from the Taylor bubble film where a relatively uniform film thickness is reached because of the bubble curvature on both ends [15].

3.2. Liquid film thickness and comparison with existing results

In [28], the liquid film thickness reaches a plateau, $\delta_{l,c}$ at high Reynolds numbers with the circular channel. This phenomenon is also seen in [10] with Taylor bubble film measurement and a square channel, in which the channel corner and center thickness are both measured and reach a plateau with high Re_D numbers (using the hydraulic diameter). Applying MEMS to manufacture the OHP, both circular and square channels have been tested and a constant thermal conductance regime has been observed [32]. They also show that the square channel in general has a larger thermal conductance than the circular channel. Here, our CFD results for the peripheral averaged slug-deposited film thickness are presented.

The results for four inlet velocities listed in Table 1, are shown in Figs. 6(a) to (c). These results are compared with $\delta_{l,c}$. In Fig. 6(a), the peripheral averaged film thickness is presented where the bubble head reaches $z = 20$ mm. Starting from the bubble head, the film thicknesses decrease axially until the pinning location is reached. The film with a higher velocity has a steeper profile, potentially caused by a larger shear stress. The interface curves more in the axial direction to balance the larger shear stress, leading to a smaller axially averaged thickness. All curves intersect near $z = 14$ mm. The slug-deposited film thickness has a steeper axial profile than Taylor bubble film, which is seen in both circular simulation [28] and experiments [33].

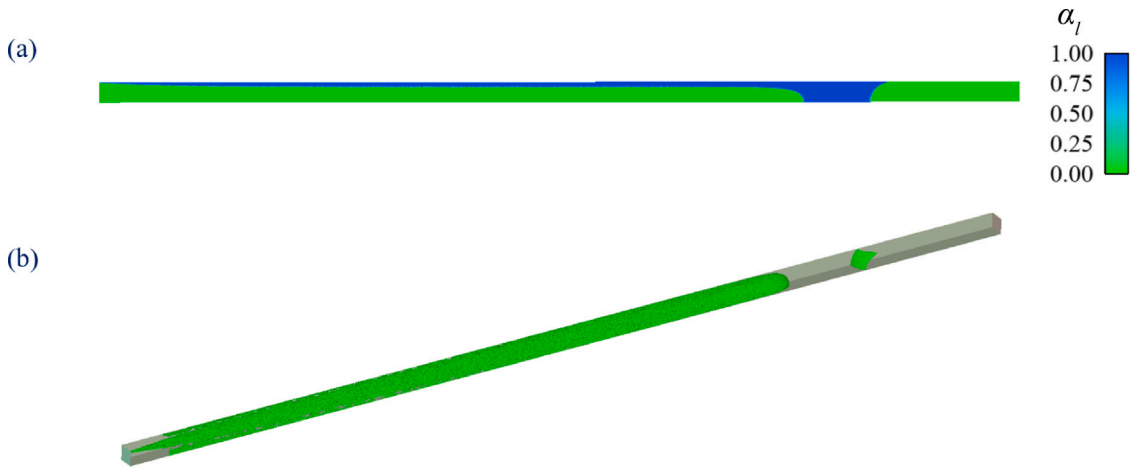

Fig. 3. (a) Snapshot of distribution of the liquid volume of fraction in the axial, oblique plane, and (b) the slug front and rear menisci topology and gas phase distribution upstream showing some dry patches (depinning). This is a snapshot of an animation (video) which can be found in Supplementary Material B.

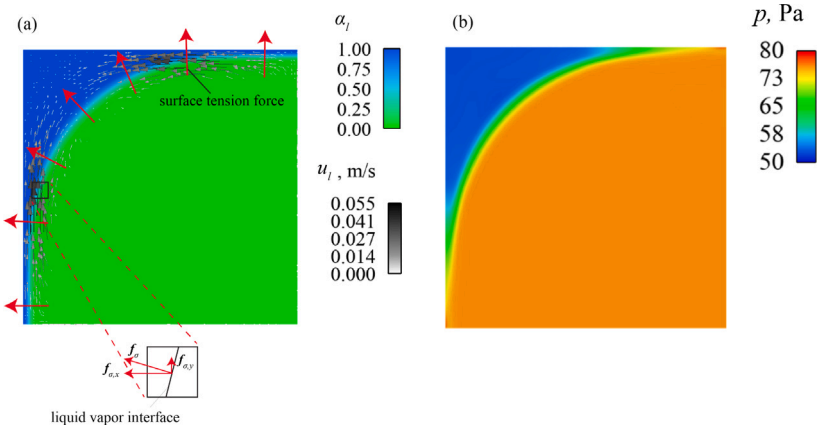

Fig. 4. (a) Phase distribution and liquid velocity vector in the peripheral plane, with an average inlet velocity of 0.5 m/s. This cross-section is taken at the peripheral plane 1 W upstream away from the tip of the meniscus. The vectors represent the liquid velocity field. The red arrow illustrates the direction of the liquid–vapor interfacial forces. (b) Pressure distribution in the liquid and gas phases. This is a snapshot of an animation (video) which can be found in Supplementary Material B.

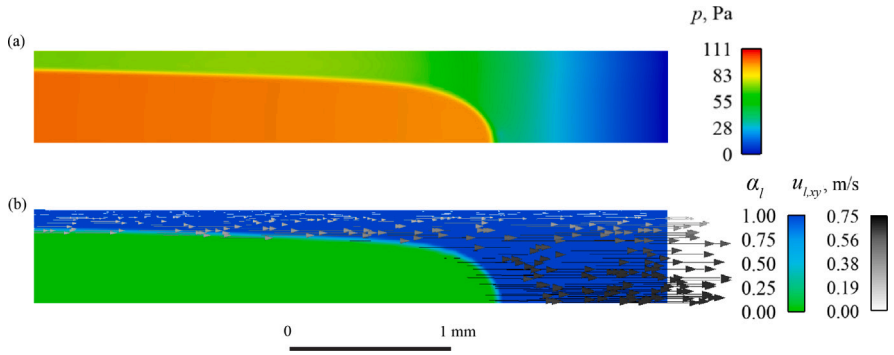

Fig. 5. (a) Axial, oblique plane liquid film pressure distribution, showing lower pressure downstream, and (b) the corresponding liquid velocity vector field and liquid volume of fraction distributions showing a nearly parallel flow, where the axial location of the tip of the meniscus z = 7 mm.

Unlike the circular cross-section films, the square channel has a non-uniform peripheral distribution. Fig. 6(b) shows this local film distribution for four different velocities, at z = 14 mm. The channel corner thickness is similar for the different velocities. At the channel center, the cases with higher velocities have larger film thicknesses. The film thickness at the channel center $\delta_{l,\mathrm{ctr}}$ is as thin as 5 to 10 μm. Similar results have been reported in [15].

As shown in the introduction, there are two different types of liquid films in OHP. (1) For the first type, The single-slug motion and its deposited liquid film are characterized by the contact line, i.e., the pinning. In operating OHP, when this film does not evaporate completely before the passing of the second slug, the pinning will disappear. (2) For the second type, the moving two slugs with a gas plug between them is the so-called Taylor bubble. Simulations with a Taylor bubble placed in between two slugs are also implemented. Fig. 6(c) shows the

variations of the predicted peripheral average (1) slug-deposited film thickness (red data) and (2) Taylor bubble film thickness (green data) as a function of slug velocity or Reynolds number. Both types of film can be seen in either 1-D-HMM simulations [9] or experiments [8]. The difference between these two liquid films is illustrated in Fig. 1. The circular channel results (yellow data) from [28] are also shown.

In Fig. 6(c), similar to the circular channel, the (2) Taylor bubble film thickness (green data) also reaches a plateau at high Reynolds numbers. However, for the (1) single slug-deposited film, the axially and peripherally averaged liquid film thickness (red date) decreases as the liquid velocity (Re_D) increases. This phenomenon can also be seen in Fig. 6(a). Since both two types of films can be found in FPOHP, the spatial average of the film thickness of these two types of films $\delta_{l,sc,c}$ (the green dash curve) is evaluated based on their spatial occupancies in 1-D HMM simulation in Section 8. In the 1-D HMM simulation, a film is identified as a single slug-deposited film if a dried region is found next to the film; otherwise, it is identified as a Taylor bubble film. The 1-D simulation shows that slug-deposited film covers 85% of the total liquid film region, which makes effective film thickness $\delta_{l,sc,c}$ closer to the slug-deposited thickness [red dots in Fig. 6(c)]. The ratio of square channel film thickness $\delta_{l,c,sc}$ to the constant circular film thickness $\delta_{l,c}$ is

$$a_\delta = \frac{\delta_{l,c,sc}}{\delta_{l,c}} = 1.07, \tag{14}$$

i.e. the peripherally, axially averaged square channel film thickness is 7% larger than circular film thickness if a high Reynold number is achieved. More film thickness simulation results with peripheral variations are shown in Supplementary Materials A and compared with the experiments of [10].

4. Non-isothermal simulation heat transfer results

In the non-isothermal simulation, Eq. (6) is applied with the phase change model and heat transfer between phases, and the thermophysical properties are used. More details about simulations are given in Section 2.

4.1. Three regions: meniscus, transition, and dry-out patched

In Fig. 7, the isosurface of liquid volume of fraction $\alpha_l = 0.5$ is shown, with the green region marking α_l smaller than 0.5 at any radial location, which is considered as the dry-out region. The blue region is the liquid slug. The film domain can be divided into three axial regions: the meniscus (bubble head), the transitional, and the dry-out patched regions. The meniscus region has an identifiable topology, and the liquid film thickness is too large to transfer heat by conduction effectively. The transition region has a relatively thin film with large conductive heat transfer. Local dry-out patches also appear, as shown in Fig. 1(b) and in [12], and the heat transfer is hindered by dry-out regions (Section 4.3. The flat film region in Fig. 1(a), could not be identified from a short-domain film deposited simulation.

4.2. Liquid-film temperature distribution and flow under evaporation

Fig. 8 shows the temperature contours of both the peripheral plane and oblique axial plane. It shows that the contour with $T = 300$ K is close to the liquid–vapor interface. The contours at the channel corner suggest that some heat is stored as sensible heat, which is waiting to be used for the heat of evaporation.

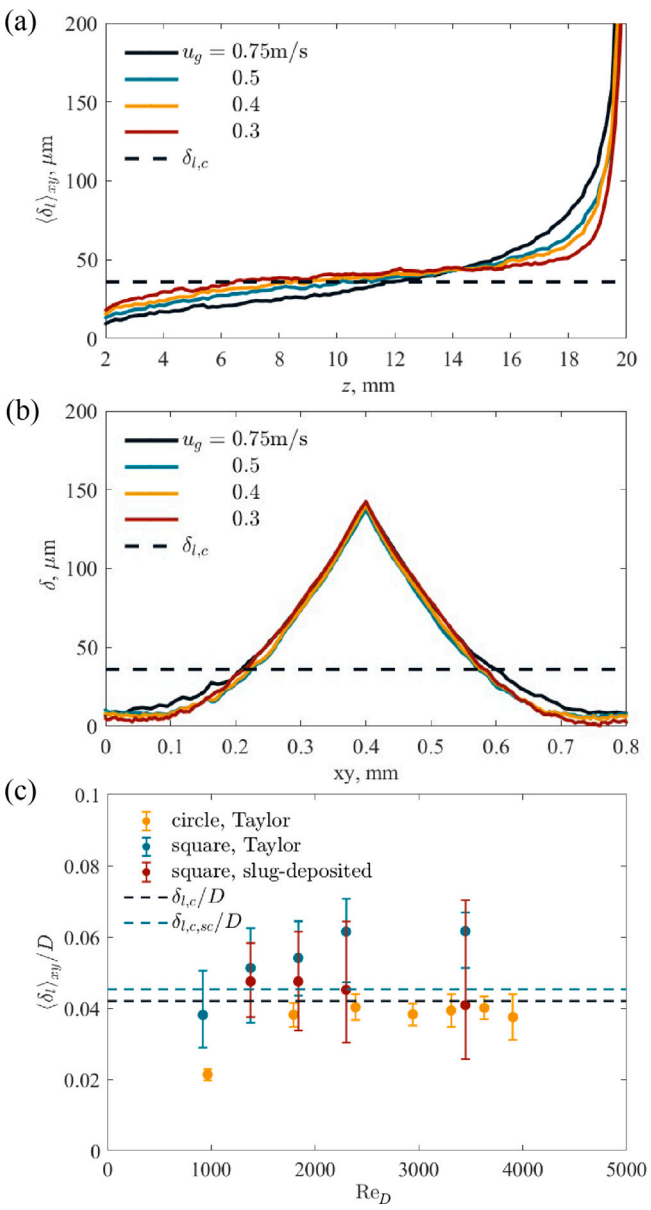

Fig. 6. (a) Peripheral average of single slug-deposited film thickness versus the axial location. (b) Liquid film thickness of the peripheral plane, at $z = 14$ mm. Locations $xy = 0$ and 0.8 mm are the channel centers, $xy = 0.4$ mm is at the channel corner. (c) The predicted peripheral–axial averaged thickness of both Taylor bubble film and single slug-deposited film versus Reynolds number, and compared with the peripherally and axially averaged film thickness in both circular $\delta_{l,c}$ and square channel $\delta_{l,c,sc}$ [28] when critical Reynolds number is reached. The error bars represent the axial variations.

4.3. Peripheral-averaged thermal conductance

Under local equilibrium, the total heat flow is used in liquid film evaporation, and the phase-change mass flux at the interface is

$$\dot{m}_{lg} = \frac{h(T_w - T_{lg})}{\Delta h_{lg}}, \tag{15}$$

where h is the total, local heat transfer coefficient through a wall location, T_w is the local wall temperature, and Δh_{lg} is the heat of evaporation. There is no thermal resistance in the gas, i.e., $T_g = T_{lg}$. The local conductive film heat transfer coefficient (specific conductance G/A) is defined as

$$\frac{G_k}{A} = h_k = \frac{k_l}{\delta_l}, \tag{16}$$

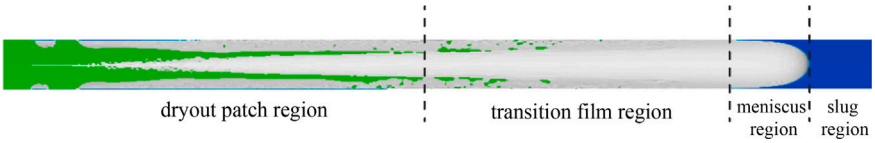

Fig. 7. Isosurface of liquid volume of fraction $\alpha_l = 0.5$, at the diagonal plane, signifying three axial regions. Blue indicates liquid slug, and green indicates dry regions. This is a snapshot of an animation (video) which can be found in Supplementary Material B.

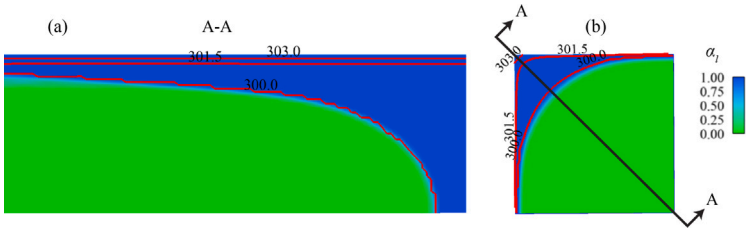

Fig. 8. Temperature contours of (a) the oblique axial plane, (b) the peripheral plane 5 mm upstream from the bubble head, subject to constant wall heat flux $q = 0.7$ W/cm^2.

where k_l is the liquid thermal conductivity, and δ_l is the local film thickness. To examine the roles of conductive liquid film heat transfer and phase change heat transfer, we apply local heat transfer balance. Using the constant heat flux condition in the simulations, the total heat transfer coefficient is

$$\frac{G}{A} = h = \frac{q}{T_s - T_{lg}}. \tag{17}$$

To observe the difference between the total heat transfer coefficient and the conductive film heat transfer coefficient, the peripheral spatial average of each coefficient is calculated respectively.

The peripheral spatial average of h_k, $\langle h_k \rangle_{xy}$, is defined as a peripheral average of the inverse of the liquid film thickness, $\langle \delta_l^{-1} \rangle_{xy}$, multiplied by the liquid film thermal conductivity,

$$\langle h_k \rangle_{xy} = k_l \langle \delta_l^{-1} \rangle_{xy}. \tag{18}$$

where $\langle\ \rangle_{xy}$ is the peripheral average of a variable. Fig. 9 shows the geometry and variables used in calculating $\langle \delta_l^{-1} \rangle_{xy}$

$$\langle \delta_l^{-1} \rangle_{xy} = \frac{1}{W} \int_0^W \frac{1}{\delta_l(y_0)}\, \mathrm{d}y_0, \tag{19}$$

where W is the square channel width, and the diagonal connecting upper-left vertex to the lower-right vertex is a line of symmetry. Thus, only one side wall of the square channel is needed for integration. (W, y_0) is a location on the side wall. The interface is evaluated by a function $f(x)$, and the local film thickness $\delta_l(y_0)$ is defined as the shortest distance from this location (W, y_0) to the interface, i.e.,

$$\delta_l(y_0) = l_{\min}(y_0) = \min[(W - x)^2 + (f(x) - y_0)^2]^{1/2}. \tag{20}$$

When there is a dry-out, the interface is close to the channel wall and the inverse of the local film thickness $\delta_l(y_0)^{-1}$ will become extremely large. A ceiling a_d is used to define dry-out locations, and the inverse of the film thickness $\delta_l(y_0)^{-1}$ is set to zero, i.e. the local film conductance is zero. This can be expressed with a Heaviside function,

$$\delta_l^{-1}(y_0) = H[a_d - \delta_l(y_0)^{-1}]\delta_l(y_0)^{-1}, \tag{21}$$

where $H(x)$ is the Heaviside function. Thus, combining Eqs. (18), (19), (20), (21), the conductive heat transfer coefficient$\langle h_k \rangle_{xy}$ is

$$\langle h_k \rangle_{xy} = \frac{k_l}{W} \int_0^W H[a_d - \delta_l(y_0)^{-1}]\delta_l(y_0)^{-1}\, \mathrm{d}y_0. \tag{22}$$

Similarly, the peripheral averages of total heat transfer $\langle h \rangle_{xy}$ is

$$\langle h \rangle_{xy} = \frac{q}{W} \int_0^W [T_s(y_0) - T_{lg}]^{-1}\, \mathrm{d}y_0. \tag{23}$$

Fig. 10(a) shows the variations of the peripheral-average film thickness for two different axial locations of the bubble-tip. The peripheral average of the total heat transfer coefficient and conductive heat transfer coefficient vary axially due to the axial variations of the film thickness.

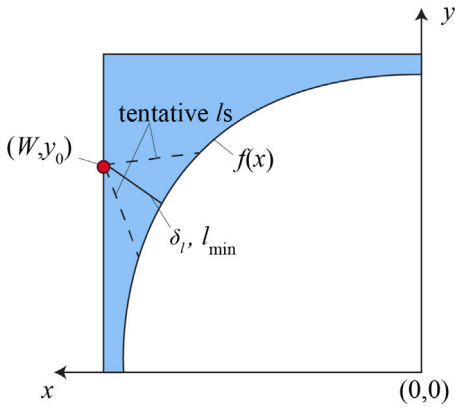

Fig. 9. Illustration defining the variable liquid film thickness δ_l and the shortest distance between the wall and meniscus.

Fig. 10(b) shows the divisions of the constant wall heat flux q into film conduction, slug convection, and dry-out waste. Before the bubble head comes, all the wall heat flux goes to slug convection and is stored as sensible heat in the liquid. Some of the sensible heat will be used for film evaporation after bubble tip arrives. The sudden increase of the film conduction around the bubble head region is potentially caused by local thermal nonequilibrium. Overall, slug convection is the dominant heat transfer mechanism before the arrival of the bubble-tip, while film conduction is the dominant heat transfer mechanism after bubble-tip reaches a certain location.

The heat transfer coefficient of these two bubble-tip locations are shown in Fig. 10(c). Eq. (17) gives the total heat transfer coefficient h, while Eq. (16) gives the conduction heat transfer coefficient h_k, and the difference between h and h_k is designated as the convective heat transfer coefficient h_u if the dry-out region is ignored. In the transition and bubble head regions, from upstream to downstream, the film thickness increases and the conductive heat transfer coefficient $\langle h_k \rangle_{xy}$ (green curves) decreases. As it reaches the slug region, the total $\langle h \rangle_{xy}$ is nearly equal to the convective $\langle h_u \rangle_{xy}$. The conductive heat transfer coefficient vanishes in the slug, while the convective dominates. In Eq. (21), a_d is introduced to define the dry-out region. With the vapor temperature constraint Eq. (2), the energy is not conserved at that location under constant heat flux. This is shown as the red area in Fig. 10(b). The corresponding equivalent dry-out heat transfer coefficient is the red curve shown in Fig. 10(c). In Fig. 7, large dry-out patches appear near the pinning location. The dry-out region is

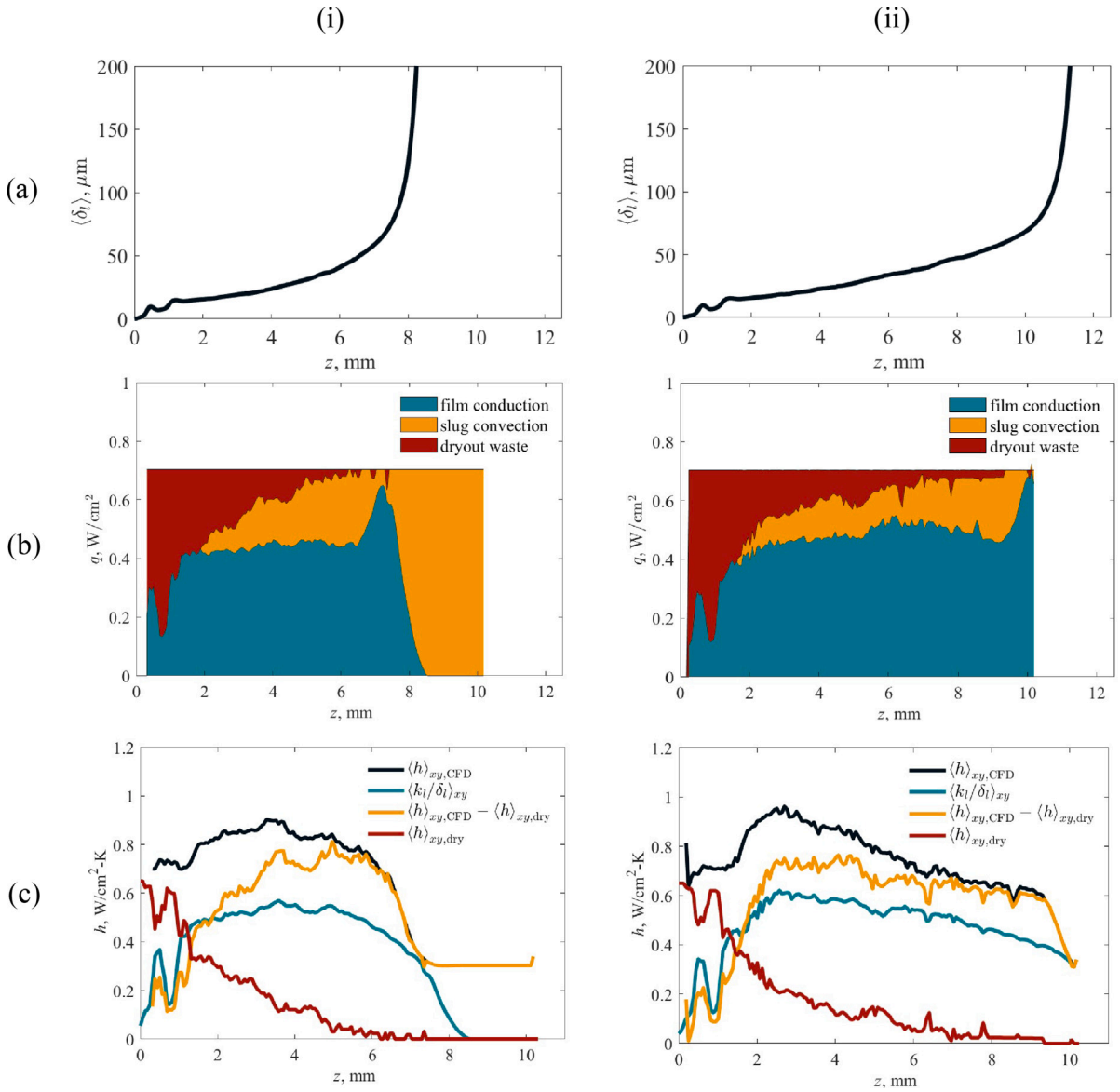

Fig. 10. When the bubble tip is at (i) z = 8.4 mm and (ii) 11.4 mm, (a) axial variations of the peripheral-averaged film thickness; (b) area of contribution division among heat transfer mechanisms; (c) peripheral-averaged heat transfer coefficients for slug velocity. The results are for u_l = 0.5 m/s and q = 0.703 W/cm^2, from Eqs. (22) and (23). The heated region ends at z = 10.25 mm.

caused by the depinning, which is explained in Section 3, and the film evaporation. Since there is a decent amount of liquid stored around the channel corner, the dry-out contribution does not increase as much between the two times. Figs. 11(a) and (b) show the axial variations of the volumetric evaporation rate and evaporation heat tranfer rate compared with the prescribed surface heat flow. The evaporation rate does not reach its maximum where the heat transfer coefficients are their maxima. The liquid motion (convection) carries sensible heat downstream, especially around the wall vicinity, as shown in Fig. 5(b). Thus, some surface heat flow is stored as sensible heat until it is used in film evaporation when the bubble tip (liquid–vapor interface) reaches downstream locations. Then at some axial locations, the evaporation heat rate is higher than the prescribed heat flux. This observation also highlights the role of convective heat transfer (sensible heat carried by the liquid motion).

In Fig. 12, $\langle D/\delta_l\rangle_{xy}$ is defined as the scaled peripheral-average inversed film thickness (green solid curve), based on Eq. (22) where we take the inverse first and then take the spatial average. $\langle D/\delta_l\rangle_{xy}$ is an accurate representation of the thermal conductance of local liquid film in the square channel. $D/\langle\delta_l\rangle_{xy}$ is defined as the inverse of the scaled average film thickness (black solid curve), where we take the peripheral average first and then take the inverse. $D/\langle\delta_l\rangle_{xy}$ reflects the thermal conductance of the liquid film in a circular channel with an equivalent liquid film thickness. $D/\langle\delta_l\rangle_{xy}$ is accurate for calculating the film conductance in circular channels due to its axisymmetric geometry but not for square channels. $D\langle h\rangle_{xy}/k_l$ (gold solid curve) is defined as the scaled total heat transfer coefficient, which is directly from the CFD calculation. The black broken line is $D/\delta_{l,c}$ using the constant Taylor bubble film thickness from [28]. In the transition region, 5 mm $\le z <$ 9 mm, $\langle D/\delta_l\rangle_{xy}$ is much larger than $D/\langle\delta_l\rangle_{xy}$, suggesting that the square channel has a large specific thermal conductance due to its peripheral non-uniform film thickness. Thus, the square channel has a better heat transfer performance than the circular channel given the same average film thickness.

The axially varying $D\langle h\rangle_{xy}/k_l$ and $\langle D/\delta_l\rangle_{xy}$ are averaged and presented by the green and gold broken lines in Fig. 12 and designated as $D\langle h\rangle_{xyz}/k_l$ and $\langle D/\delta_l\rangle_{xyz}$. The peripheral varying film thickness causes a major difference between $\langle D/\delta_l\rangle_{xyz}$ and $D/\langle\delta_l\rangle_{xy}$, which is

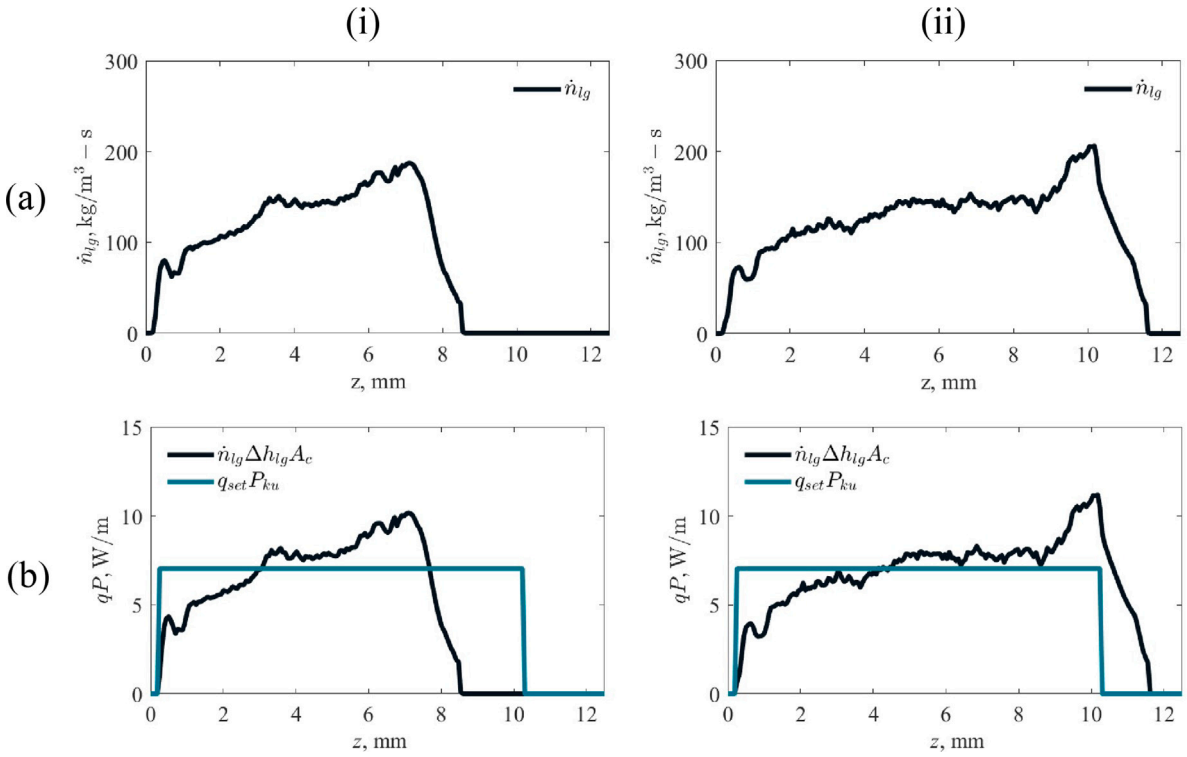

Fig. 11. Axial variations of average (a) volumetric evaporation rate, and (b) the surface heat flow rate per unit length (P is the channel periphery) and evaporation heat transfer per unit length (A_c is the cross-section area), with the bubble tip located at (i) z = 8.4, and (ii) 11.4 mm.

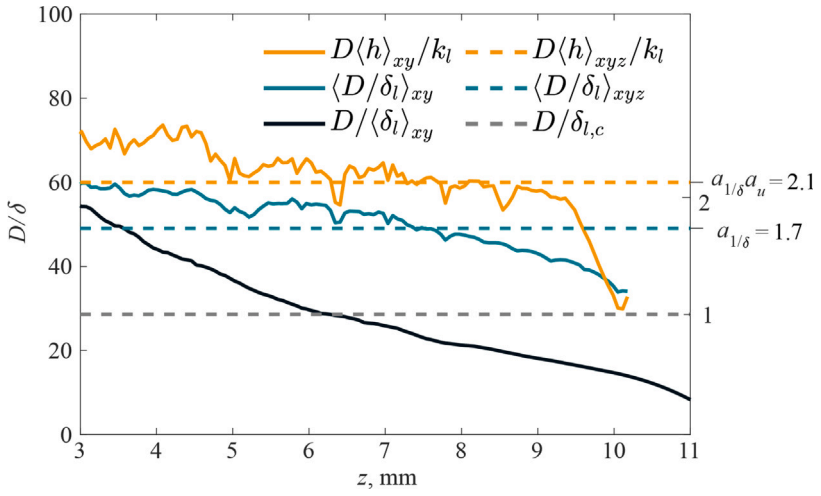

Fig. 12. Axial variations of the scaled inverse liquid film thicknesses. The gold curve and broken line represented the total heat transfer coefficient by CFD. The green curves show the peripheral averaged inverse CFD film thickness distribution. The black curve is based on the CFD peripheral-averaged film thickness and the gray dash line is calculated by the correlation at high Laplace number from [28].

presented as an axially averaged value. Liquid convection also makes a considerable contribution to the heat transfer, causing the difference between the gold and green broken line. To quantify these differences, we define two corrections $a_{1/\delta}$ (for non-uniformity of square channel film) and a_u (for convection)

$$a_{1/\delta} = \frac{\langle D/\delta_l\rangle_{xyz}}{D/\langle\delta_l\rangle_{xyz}} = 1.72, \tag{24}$$

$$a_u = \frac{D\langle h\rangle_{xyz}/k_l}{\langle D/\delta_l\rangle_{xyz}} = 1.24. \tag{25}$$

These two corrections are used to modify the square channel thermal conductance calculations based on a Taylor thickness $\delta_{l,c}$. Here we assume these constants can be used for other fluids and conditions for the square channel OHP, which is explained in Section 7.

5. Liquid-film based internal OHP thermal conductance

5.1. Ideal OHP conductance

A simple model for the OHP conductance, first developed in [28], is adopted and modified in this study for a square channel by CFD predictions and experiments. The analytic model poses an upper limit on the thermal conductance (lower limit on thermal resistance), based on the assumption of complete film coverage lining the OHP channel. We also assume that the heat transport in OHP is dominated by evaporation and condensation through the thin liquid film (latent heat transfer).

Using these assumptions, and considering the surface areas available for evaporation and condensation (the outer surfaces of the channels), the expression for an ideal, upper-limit, square channel OHP conductance is given by

$$G_{\delta_l} = \frac{k_l}{\delta_{l,sc,c}} \left(\frac{1}{A_e} + \frac{1}{A_c} \right)^{-1}, \tag{26}$$

where A_e and A_c are the channel wall areas in the evaporator (heater) and condenser (cold plate) sections, respectively. The specific conductance of the liquid film $k_l/\delta_{l,sc,c}$ is modified for the square channel geometry, based on the correlation for circular channels ($\delta_{l,c}$). The effective film thickness for heat transfer in the square channel is

$$\delta_{l,sc,c} = \frac{a_\delta}{a_u a_{1/\delta}} \delta_{l,c}, \tag{27}$$

where $a_{1/\delta}$ accounts for the peripheral variation in the square channel film thickness, and a_u describes the contribution of liquid convection to the heat transfer in the liquid film [Eqs. (24), (25)]. Finally, a_δ accounts for the spatial occupancy of the two different types of liquid film in 1-D simulations and CFD [Eq. (14)]. Thus, these three coefficients describe the deviation of the effective film thickness for heat transfer in a square channel when compared to a circular channel. The calculation of each coefficient is described in more detail, in Sections 3 and 4.

The constant liquid film thickness $\delta_{l,c}$ in a circular channel is calculated by the empirical relation developed by [34], which described the thickness of the Taylor-type liquid film as a function of the plug Reynolds number. At high Reynolds number flow, the liquid film reaches a constant thickness independent of the slug velocity, given by

$$\delta_{l,c} = \frac{106 D \mathrm{La}_D^{-2/3}}{1 + 576 \mathrm{La}_D^{-2/3} + 7765 \mathrm{La}_D^{-0.672} - 5914 \mathrm{La}_D^{-0.640}}, \tag{28}$$

under the constraint that $\mathrm{Re}_D > 2000$. The Laplace number describes the fraction of surface tension to diffusivity with the diameter used as the characteristic length, and this is given in Eq. (13). Since the Laplace number depends on the fluid properties, the simple model we propose can also be extended to other working fluid configurations in OHPs. This correlation applies only in the high heat flux OHP limit (when slug velocities are largest), so G_{δ_l} represents an upper bound on the OHP conductance that could only be reached at the highest heating input. Eq. (28) can also be approximated as proposed in [28] by

$$\delta_{l,c} \approx 120 D \mathrm{La}_D^{-2/3}. \tag{29}$$

5.2. Incorporating filling ratio and liquid slug convection

Eq. (26), the ideal OHP conductance, assumes complete film coverage within the OHP. In reality, a fraction of the total OHP volume is occupied by moving liquid slug regions, where the specific conductance is given by h_l, which in our case, is about half as large as the specific film conductance in the square channel, $k_l/\delta_{l,sc,c}$. Considering a parallel, 1-D heat flow to liquid slugs instead of solely to the liquid film gives the modification below for G_{δ_l}

$$G_{\delta_l,\alpha_l'} = \frac{k_l}{\delta_{l,sc,c}} \left\{ 1 - \alpha_l' \left[1 - \frac{h_l}{k_l/\delta_{l,sc,c}} \right] \right\} \left(\frac{1}{A_e} + \frac{1}{A_c} \right)^{-1}, \tag{30}$$

where α_l' is the modified filling ratio. The modified filling ratio represents the fraction of the whole domain that is occupied by the liquid slugs (instead of the liquid films). In other words, the total OHP fill ratio α_l is divided into regions of liquid slug (α_l') and regions of liquid film. Considering the liquid volume occupied by the liquid films, α_l and α_l' are related by

$$\alpha_l = \alpha_l' + \frac{4\delta_{l,sc,c}}{D}(1 - \alpha_l'), \tag{31}$$

where $\delta_{l,sc,c} = a_\delta \delta_{l,c}$ and the constant film thickness $\delta_{l,c}$ is given by Eqs. (28) or (29).

In this study, we estimate the value of h_l of liquid slugs in two ways. First, we relate the average liquid slug velocity u_l in OHP to the applied heat flux q in the evaporator using the correlation developed in [28] which considers the minimum length of liquid slug $L_{s,o}$ required to replenish the thin liquid film during evaporation,

$$u_l = \frac{4qL_e^2}{\rho_l D L_{s,o} \Delta h_{lg}}, \tag{32}$$

where we assume $L_{s,o} \approx 1.75D$ for the square channel geometry. This expression is idealized for an OHP operating in a unidirectional regime, which can be achieved with vertical orientation or through the use of check valves [35]. In an oscillatory regime, where liquid slugs are continuously reversing travel direction in the channels such as with the horizontal OHP considered here, Eq. (32) will overestimate the averaged slug velocity. With known average liquid slug velocity, the heat transfer coefficient to moving liquid slugs can be predicted using the Nusselt number correlation for developed liquid flow in a square channel, and this also accounts for the transitional regime common in OHPs. This Nusselt number correlation is [36]

$$\langle \mathrm{Nu} \rangle_D{}^{10} = \langle \mathrm{Nu} \rangle_{D,l}{}^{10} + \left[\frac{\exp(\frac{2200 - \mathrm{Re}_D}{365})}{\langle \mathrm{Nu} \rangle_{D,l}{}^2} + \frac{1}{\langle \mathrm{Nu} \rangle_{D,t}{}^2} \right]^{-5}, \tag{33}$$

where standard correlations for the laminar ($\langle \mathrm{Nu} \rangle_{D,l} = 3.61$) and turbulent Nusselt numbers have been used for the square channel. The average heat transfer coefficient can then be readily calculated using $\langle h_l \rangle = k_l \langle \mathrm{Nu}_D \rangle / D$. The other method by which we have incorporated the single-phase convection to the liquid slugs is by averaging the steady-state value of $\langle h_l \rangle$ as predicted by the 1-D HMM simulations described in Section 8. As mentioned earlier, the value of $\langle h_l \rangle$ that is predicted using the above correlation is likely to be an overprediction compared to the 1-D HMM simulations due to the assumption of a unidirectional-type flow in the former. Thus, if available, using the value predicted by simulations provides a closer agreement of the model with experimental data.

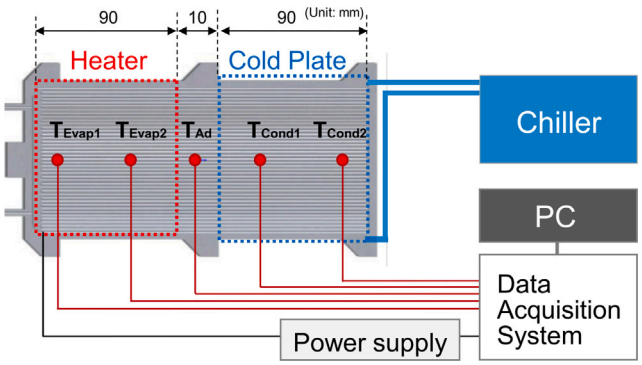

Fig. 13. Schematic of the FPOHP experiment setup [9]. The evaporator (Evap), adiabatic (Ad), and condenser Cond) sections, and the location of thermocouples, are shown.

6. FPOHP experiments

FPOHP tests were conducted to obtain the experimental data at various heat load inputs. Fig. 13 shows a schematic diagram of the experimental setup. The specifications of the OHP are listed in Table 2. The OHP was made of AlSi10Mg by additive manufacturing using the direct metal laser sintering method. The total width, length, and thickness of the OHP are 90, 200, and 3.8 mm, respectively. The channel has a square cross-section with a height and a width of 1.0 mm. The total turn number is 42. R-134a was used as the working fluid. The filling ratio of R-134a was $\alpha_l = 0.45$ of the internal channel volume.

The heat input is applied by a Kapton heater (OMEGA, KHA-303/5-P) and a DC power supply (Sorensen XHR 300-2). The condenser section is mounted on the cold plate via silicon-based thermal interface

Table 2
Specifications and conditions of the FPOHP used in the experiment.

Wall material	AlSi10Mg
α_l	0.45
Working fluid	R-134a
L_e	90 mm
L_a	10 mm
L_c	90 mm
Total thickness	3.8 mm
$D = W$	1 mm
Turns	42

material. The cold plate is connected to a chiller which provides constant sink temperature at 10 °C. Five type-E thermocouples were used for temperature measurement. Thermocouple locations are shown in Fig. 13. Temperatures were recorded every 2 s using the PC connected to the data logger (Keysight 34972 A). The whole system is covered with thermal insulation. The flow channels were ensured to be leak-tight before charging, and there was no fluid leakage even under the high pressures (several atm) within the channels during the operation. We note that the individual tests were not repeated here; however, at each heat input, the temperature data was taken with a time-average of 10 min in the steady-state. All experiments are conducted at a horizontal orientation where the effect of gravity is considered to be negligible. The experimental set-up of the additively manufactured FPOHPs is also reported in [37] for a similar square channel, and in [38] for an FPOHP with embedded circular channels and experimental uncertainties associated with the equipment are discussed there.

The thermocouples are only placed on the central axis since the major temperature gradient (controlling the FPOHP thermal conductance) is in the axial (horizontal) direction, and the lateral temperature changes are minor. This is confirmed by the 1-D HMM simulations with the 3-D conduction effect discussed later. In addition, these thermocouple temperatures fluctuate with time, so the 10-minute steady-state average of the temperatures smooths any lateral temperature variations.

Heat input Q was applied at 10, 20, 30, 40, 50, 60, 80, 100, 120, 140, 160, 180, 200, and 210 W to observe performance variation under a wide heat input range. Thermal conductance was calculated using the average temperature difference between the evaporator and condenser and dividing by the applied heat input. The Type-E thermocouples used have a 1 °C measurement error. This means the temperature difference prediction used to calculate thermal conductance has a 2 °C measurement error. The error is thus propagated into the thermal conductance, and this uncertainty falls to about 10% in the high-heat flux limit which is compared to the analytic model. The calculated thermal conductance is presented in Fig. 14, along with an uncertainty band based on the thermocouple measurement error. The thermal conductance is lowest at the smallest heat input of 10 W and increases as the heat input is increased. The maximum thermal conductance FPOHP achieved was 18.0 W/K at a heat input of 210 W. As a general trend, the thermal conductance of FPOHP with square channels was lower than the previously presented thermal conductance of FPOHP with circular channel at lower heat input (below 80 W), but it became higher than circular channel's conductance at higher heat input (above 100 W) [9]. In this case, the thermal conductance at 200 W was 17% higher in the square channel FPOHP test.

Since the square and circular channels have identical hydraulic diameters, the areas available for heat transfer (A_e and A_c) in the square channel are larger by $4/\pi$ (27%) compared to the circular case, due to the larger perimeter in the former. When the FPOHP thermal performance is compared at the same heat flux q accounting for the areal differences, the thermal conductance is about 24% larger for the square channel compared to the circular channel in the high heat flux limit. Since this difference is close to the advantage created by the longer channel perimeter of square channels, it implies that the effective film thickness for both square and circular channels are similar in this experiment, despite the peripheral non-uniformity and convection advantages in the square channel [see Eq. (26)]. These differences in effective film thickness between the square and circular channels may be related to the flow regime (unidirectional versus oscillatory) or the dry-out behaviors (especially in the square channel where thin-film regions are more extensive) and are left for future study. However, we note that other authors have reported a larger FPOHP thermal conductance advantage (> 27%) using the square channel when compared to a circular channel with the same hydraulic diameter, in experiments [1].

7. Comparison of experiment with ideal conductance model

Fig. 14 compares the ideal conductance predicted using the various corrections introduced in Section 5 to the related experimental results. The corrections made for the conductance prediction G are summarized in Table 3.

The turquoise line in Fig. 14 is the ideal OHP conductance, where the entire OHP inner channel surface is assumed to be fully covered by evaporating/condensing liquid film following Eq. (26). Then, the single-phase convection to liquid slugs is considered using the modified filling ratio with Eq. (30), where h_l was estimated using the 1-D HMM averaged, high-heat load $\langle h_l \rangle$ (black line), which brings the upper limit prediction to better agreement with the experiment. From the 1-D simulation, $\langle h_l \rangle$ = 730 W/m^2-K. In all the upper limit predictions, the relevant fluid properties are evaluated at the average temperature

Table 3
Summary of modified, ideal square channel FPOHP thermal conductance G, starting with the circular channel film thickness, adding the square cross-section and the slug surface coverage.

Modification	G
Ideal, circular channel [28]	$G_{\delta_l} = \frac{k_l}{\delta_{l,c}}\left(\frac{1}{A_e}+\frac{1}{A_c}\right)^{-1}$, $\delta_{l,c} \approx 120 D \mathrm{La}_D^{-2/3}$
Square channel liquid film	$G_{\delta_l} = \frac{k_l}{\delta_{l,sc,c}}\left(\frac{1}{A_e}+\frac{1}{A_c}\right)^{-1}$, $\delta_{l,sc,c} = \frac{a_\delta}{a_u a_{1/\delta}}\delta_{l,c}$ $a_\delta = 1.07, a_u = 1.24, a_{1/\delta} = 1.72$
Filling ratio and liquid slug convection	$G_{\delta_l,\alpha_l'} = G_{\delta_l}\left[1-\alpha_l'\left(1-\frac{h_l}{k_l/\delta_{l,sc,c}}\right)\right]$

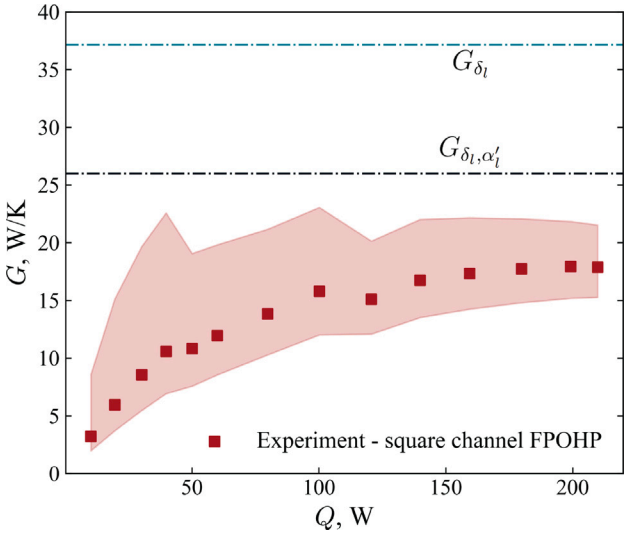

Fig. 14. Comparison of the experimental FPOHP conductance results with the predicted upper limits. The green line is based on complete film coverage, while the black line has been adjusted for convection to moving liquid slugs by using the modified filling ratio α_l' and 1-D HMM simulation results. The light red band is to indicate the experimental uncertainty.

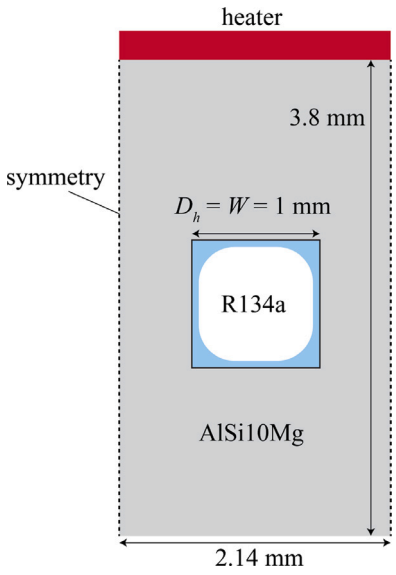

Fig. 15. Schematic of the cross-section of the FPOHP as tested in the experiment, and as modeled using the 1-D HMM simulations.

between the evaporator and condenser (at the highest tested heat input).

We note that the predictive power of the analytic model for the square channel FPOHP may be limited by using the CFD-predicted corrections for circumferential inhomogeneity $a_{1/\delta}$ and liquid convection a_u from the simulation using a single fluid and operating condition. However, experiments [10] and simulations [15] have suggested that the circumferential geometry trends do not change significantly with various working fluids. For example, in Fig. A.1. of the Supplementary Materials, ethanol, water, and R-134 corner and center film thicknesses fall within the same range, and so does the ratio of $\delta_{l,\mathrm{cnr}}$ to $\delta_{l,\mathrm{ctr}}$. Convection within the thin liquid film is expected and may change depending on the fluid thermal conductivity; however, this correction is minor compared to the circumferential inhomogeneity factor. Corrections of choice may be omitted from the model, depending on the desired conditions. The constant liquid film thickness $\delta_{l,c}$ used in the model is a function of the fluid surface tension, viscosity, density, and channel size using the hydraulic diameter, through the Laplace number [Eqs. (28), (29)]. The model is suited for the high heat flux steady-state operating condition (for circular channels this is when a critical Reynolds number is reached [28]). Unsteady or transient behaviors are not captured since these phenomena can not easily be included in a thermal conductance relation, and some of these transient behaviors are irrelevant (such as the stop-over phenomena) [39].

8. 1-D heat-mass-momentum conservation simulations including 3-D conduction

The 1-D heat-mass-momentum (1-D HMM) simulation first developed by [9] is adopted for simulations of the square channel FPOHP setup that was experimentally tested, as described in Section 6. This model simulates a 1-D chain of liquid slugs and vapor plugs by solving the energy equation in the solid wall, liquid slugs, and vapor plugs. The momentum equation is solved for liquid slugs considering the frictional pressure loss in the turn sections. A heating plate is applied to the top of the solid casing in the evaporator region, and a cooling plate is at the bottom of the solid casing in the condenser region. The model simulates the fluid channels in 1-D, but the channels are thermally connected to a 3-D conduction model which simulates the heat flow laterally between channels and axially between the evaporator and condenser.

After a transient period of heating, the vapor plugs and liquid slugs in the simulation reach a steady-state oscillatory regime transferring heat primarily by liquid film conduction during vapor plug evaporation and condensation. Further details on the complete numerical model can be found in the original articles [9,35,40,41], and this model has previously shown reasonable agreement with the relevant experimental results.

The original code was developed for a circular channel. In this study, it is adopted for square channels by increasing the channel areas by a factor of $4/\pi$. Here, the hydraulic diameter is equal to the channel width, and this diameter is used for the relevant empirical fluid correlations including the evaluation of the liquid slug heat transfer coefficient [see Eq. (33)] and the frictional pressure loss. The simulation input conditions to the 1-D HMM simulation are similar to the experiment (see Section 6), and summarized in Table 2.

To decipher the negative conduction penalty caused by conduction between adjacent OHP channels, we also simulate the same geometry and configuration, but remove the 3-D conduction interaction. When this is removed, the overall OHP conductance improves, which is consistent with findings in [3]. At high heat flux, this effect diminishes, but we predict a conductance penalty approaching 3.7 W/K in the limit of high heat flux; this penalty improves the predictions of the ideal conductance when compared with experiments.

The choice of the liquid film thickness in the 1-D-HMM simulations δ_l has previously been used as a fitting parameter [9,35], but here we have used the value of 17.5 μm based on the CFD predictions described in Section 4, and predicted by Eq. (27). Thus, the effective film thickness is about twice as thin when compared to the constant, circular channel film thickness.

Fig. 15 shows a cross-sectional 2-D unit cell of the FPOHP as simulated in the 1-D HMM model (as well as in the experiment). This unit cell has peripheral symmetry but neglects the slightly wider spacing at the ends of the structure. The channels occupy about 12% of the total cross-sectional area. The heater is at the top surface, and there is an equivalent one-sided cooling plate in the condenser region.

Fig. 16 shows the comparison of the thermal conductance among the experiment, the complete 1-D HMM simulation, and the 1-D HMM simulation when the 3-D conduction is removed, as described above. The simulations were run for 300 s (with 3-D conduction) and 100 s (without 3-D conduction) so that the steady-state condition was reached. The thermal conductance was predicted based on the time-averaged temperatures of the evaporator and condenser (at steady-state) and the heat load condition. The model shows reasonable agreement with experiments using the CFD effective film thickness $\delta_{l,sc,c}$. As the heat load increases, the deviation between the 1-D HMM simulation with (black points) and without (yellow points) 3-D conduction decreases but approaches a constant of around 3.7 W/K, as demonstrated in Fig. 16. We use this conductance penalty in the next section to improve our predictions, using Eq. (34). In Fig. 17, a snapshot from the simulation during steady-state (at 290 s and heat input of 150 W) is shown. The notable features include Taylor-type bubbles (vapor plugs with no dry-out region), and slug-deposited films (adjacent to a dry-out region). We note the significant number of dry regions compared to liquid film regions; this can lower the thermal conductance, causing deviation of the experimental results from the ideal conductance model.

9. Discussion of non-ideal thermal conductance

As expected, the experimental results for the thermal conductance are below the analytically modified ideal OHP conductance G_{δ_l}. The experimental results, as well as the 1-D HMM predictions, reach only 70% of this modified ideal limit. Possible reasons for this difference are discussed in detail below.

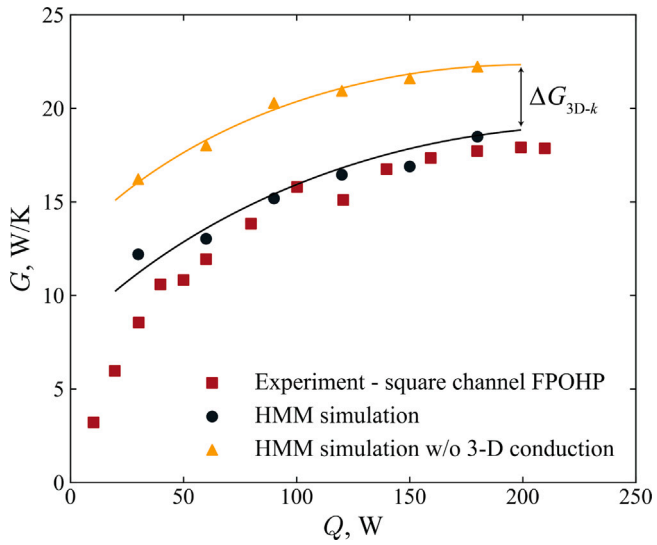

Fig. 16. Comparison of the conductance between the experimental results for a square channel FPOHP, and the 1-D HMM simulation modified for the square channel, which also includes the 3-D conduction paths in the solid-plate system (black data). The yellow data is the result when adjacent OHP channels are not permitted to thermally interact.

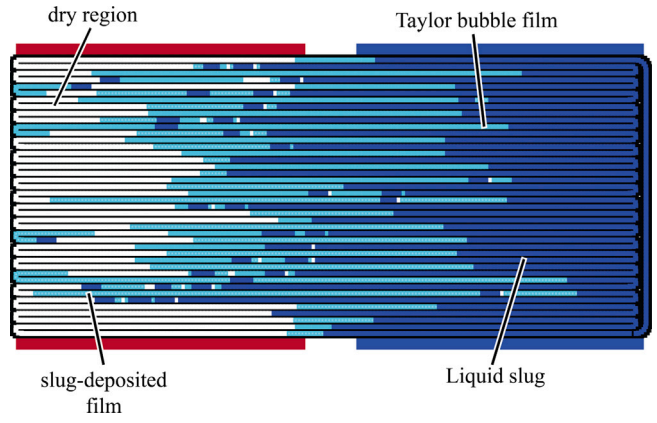

Fig. 17. Snapshot of the 1-D HMM simulation during steady state. Liquid slugs (dark blue), dry regions (white), and liquid films (light blue) are noted. The blue rectangle behind the OHP is the condenser region, while the red rectangle is the evaporator region. A significant portion of the channel volume appears dry, and this lowers the OHP conductance.

9.1. 3-D solid conduction between adjacent channels

In typical FPOHPs, a large fraction of the cross-sectional area is occupied by solid material. As mentioned earlier, [3] determined that the heat transfer between neighboring channels reduces the overall FPOHP conductance, and this has been attributed to an equilibrium effect between the adjacent OHP channels that acts to reduce the characteristic oscillation effect [4]. Using 1-D HMM simulations with and without this transverse thermal interaction between the OHP channels, we quantify the corresponding penalty on the OHP conductance for the configuration tested here. The magnitude of this effect decreases with increasing heat flux, as also verified by [3], approaching a conductance penalty of about 15% at the highest test heat flux. In this study, using the 1-D HMM simulations described in the previous section, we also estimate a conductance penalty due to this interaction and then calculate a final correction to the ideal OHP conductance G_{δ_l}, including the modified filling ratio, as

$$G_{\delta_l,\alpha_l',k} = G_{\delta_l,\alpha_l'} - \Delta G_{\text{3D-}k.} \tag{34}$$

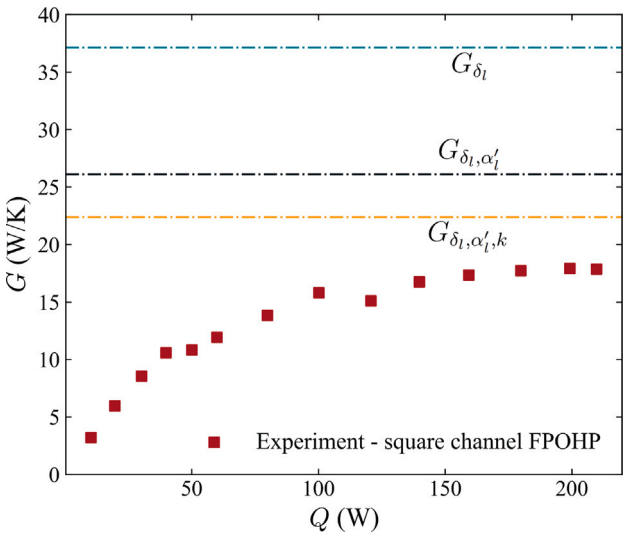

Fig. 18. Comparison of the experimental FPOHP conductance with the predicted upper limits. The green line and the black line are the same as before (Fig. 14), while the yellow line is an adjustment based on 3-D conduction made from Eq. (34) using the 1-D HMM simulation results.

The addition of this penalty to Fig. 14 brings the experimental results to closer agreement with the conductance model, and the adjusted results are shown in Fig. 18

Although bringing the model to closer agreement with the experiment, the 3-D conduction correction considered here is not comprehensive for this effect, since it is based only on the experimental specifications considered in this R-134a experiment. The analytic model establishes an upper-limit thermal conductance where this effect does not exist, and there have been some attempts to mitigate this negative transverse conduction effect [3,42]. Using the 1-D HMM simulations to determine a functional form of the conduction penalty is outside the scope of the present investigation which focuses on a baseline thermal conductance prediction.

9.2. Partial dry-out

The 1-D HMM simulations [9] and test flow visualizations [3] show that the evaporator can contain large dry regions, which have a much smaller specific conductance compared to the thin liquid film. A time-average of the 1-D HMM results during the pseudo-steady state at high heat flux reveals that around 25% of the OHP channel length is occupied by dry regions (regions with no liquid film). This is also shown in Fig. 17. The partial dry-out significantly reduces the OHP thermal conductance since the heat transfer coefficient between the wall and dry vapor is small. The presence of dry vapor also modifies the amount of liquid film in the OHP channels due to the volume constraints of the filling ratio. That is, $\alpha_l = \alpha_l' + \frac{4a_\delta \delta_{l,c}}{D}(1-\alpha_l'-\alpha_d)$ where α_d is the volume fraction of dry regions. When the presence of dry regions ($\alpha_d = 0.25$) is included in the ideal conductance model, the thermal conductance is under-predicted by about 20% compared to the experiment.

It is expected that the 1-D HMM simulation overpredicts the fraction of dry region in the OHP with square channels. Since the channel is simulated as 1-D, the dry regions are considered to have no liquid film coverage in the entire cross-section. However, as shown in non-isothermal CFD (Section 4), corner films can persist because dry-out first appears near the center of the channels away from the corner. Therefore, the liquid film in corners can contribute to heat transfer significantly, even where partial dryout has occurred.

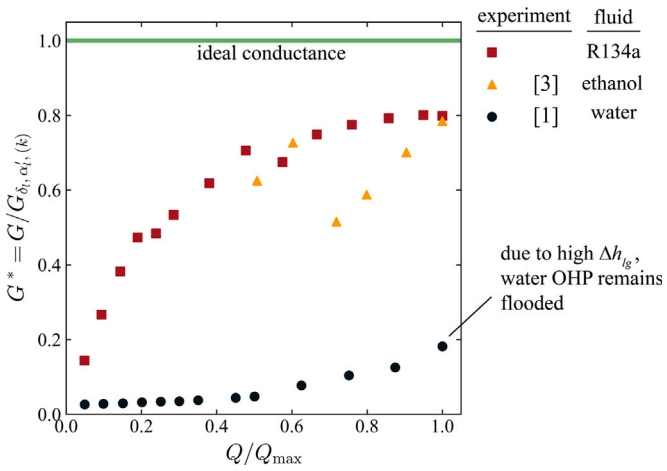

Fig. 19. The dimensionless, ideal upper limit conductance $G^* = 1.0$, with the slug coverage and 3-D conduction adjustments, compared to the results of R-134a and ethanol (red and yellow data, respectively) experiments, which reach up to 80% of their limit. Water does not reach the required heat input (remains in a more flooded regime) to approach its upper limit, as previously found [28]. The x axis is the heat input over the maximum tested condition (which varies significantly across different experiments).

9.3. Additional non-ideal thermal conductance considerations

- Continued flooding of the condenser: the 1-D HMM simulations show that even at high heat loads the condenser is still partially flooded.
- In experiments where the heating or cooling is one-sided, the uniform channel surface heat flux assumption does not hold, and heat flux to the corners and to regions between the corners will not be the same. This will affect the heat transfer rate, as the corners will have greater thermal resistance.
- The ideal, axially uniform, liquid film thickness as assumed in the model will not appear during evaporation or condensation due to the dynamics of passing, film deposited liquid slugs.

10. Comparison of ideal conductance with additional experiments using other fluids

To further validate the ideal analytic thermal conductance (or resistance) model, a comparison is made with two additional FPOHPs, one using ethanol [3] and the other using water [1]. Fig. 19 shows this comparison using a dimensionless thermal conductance determined by dividing the conductance by the ideal upper limit of the configuration, i.e.,

$$G^* = \frac{G}{G_{\delta_l,\alpha'_l,(k)}}. \tag{35}$$

For the water and ethanol experiments, the dimensionless G^* uses the convection correction only, while the R-134a experiment is also corrected for the conduction effect [subscript k in Eq. (35)]. The predicted convection correction for water and ethanol was made using Eq. (33) since 1-D HMM simulations of these configurations were not performed. In the ethanol experiment [3], a MEMS technique was used to remove solid material between adjacent OHP channels in the structure (to improve thermal conductance). Therefore, there is no need to make the additional correction for 3-D conduction effects. For the water experiment, the 3-D conduction effect was not included in the thermal conductance, as this effect could not be predicted.

The FPOHPs described here have varying geometries and configurations, so the heat input varies significantly across the experiments. As a result, the heat input has been scaled to the maximum heat input tested in the experiment, $Q/Q_{\max}$.

The result using water suggests that a very large heat load is required to sufficiently excite the liquid slug and vapor plug oscillation, and reach closer to the upper limit regime. The same result was obtained in the comparison by [28]. Water has a very large heat of evaporation Δh_{lg}, and this corresponds to small slug velocities [Eq. (32)] meaning that the water OHP is likely to be heavily flooded (liquid slugs are accumulated in the condenser region).

11. Conclusions

The 3D-printed square cross-section OHP are partially liquid-filled, embedded, continuous, meandering capillary channels connecting the heat input (evaporator) and heat extraction (condenser) sections. Once the discontinuous liquid flow begins in the form of slugs, a portion of the liquid becomes deposited as a thin liquid film due to the surface adhesion forces. In this study, we have used isothermal and non-isothermal CFD simulations to study the liquid film formed by a moving slug. For the case of the circular cross-section, this liquid film has a uniform thickness across the channel [28], while with the square cross-section, the thickness is much greater in the corner regions. The liquid film thickness grows rather slowly axially. The liquid film is formed by surface adhesion, then due to curvature capillarity, the liquid flows from the channel center to the channel corner, where the liquid pressure is lower. This results in the thinning of the film in the channel corner; however, the peripheral-averaged liquid film thickness for the square channel is close to that of a circular channel (for the same Reynolds number based on the hydraulic diameter). At high Reynolds numbers, the area-averaged film thickness is slightly smaller for the square channel.

The non-isothermal simulations allow for calculating the local and averaged heat transfer coefficient (specific conductance), and due to the peripheral film thickness variation, the average specific conductance obtained by peripheral integration of the inverse of the film thickness is larger than the conductance based on the inverse of the average film thickness. The integrated inverse of film thickness is 1.74 times the inverse of the average of the film thickness. The liquid motion in the film has a convection effect that increases the specific conductance by a factor of 1.24. Using these, a relationship for effective film thickness is proposed and used in the proposed upper limit for the OHP conductance. This ideal conductance is compared with experimental results for an OHP with a square cross-section, embedded channel, 3-D printed OHP made of aluminum alloy, with a side dimension of 1 mm, and using R-134a as the fluid with a filling ratio of 0.45. The experimental results show the commonly observed low-heat-load (heat flux) flooding regime with reduced conductance and a constant high-heat-load conductance regime (before dry-out begins) below the predicted liquid-film based upper-bound conductance. This study offers a simple, analytic relation for the ideal, internal thermal conductance of square cross-section OHP based on complete film coverage. This

relation is given $G_{\delta_l} = \frac{k_l}{\delta_{l,sc,c}} \left(\frac{1}{A_e} + \frac{1}{A_c} \right)^{-1}$, where the effective film thickness in the square channel is $\delta_{l,sc,c} = \frac{a_\delta}{a_u a_{1/\delta}} \delta_{l,c}$, and the CFD-estimated values of a_δ, a_u and $a_{1/\delta}$ are 1.07, 1.24, 1.72, respectively. The circular channel film thickness is approximated as $\delta_{l,c} \approx 120 D \mathrm{La}_D^{-2/3}$. The ideal conductance G_{δ_l} is then adjusted to consider the presence of the moving liquid slugs by accounting for their single, liquid-phase convection, and allowing for the 3-D conduction. Both of these effects reduced the ideal conductance. The modified prediction of upper bound conductance agrees well (up to 80 percent) with the experimental results. Compared with the circular OHP, the square channel FPOHP has a better predicted thermal conductance performance, due to its higher internal thermal conductance. The 3-D conduction in the plate has a negative effect, but the advantage of the internal conductance dominates in FPOHP.

CRediT authorship contribution statement

Fan Lu: Writing – review & editing, Writing – original draft, Software, Methodology, Investigation, Formal analysis, Data curation, Conceptualization. **Lorenzo Franceschetti:** Writing – review & editing, Writing – original draft, Validation, Software, Methodology, Investigation, Formal analysis, Data curation, Conceptualization. **Kyle Kippner:** Software, Investigation, Data curation, Conceptualization. **Massoud Kaviany:** Writing – review & editing, Writing – original draft, Supervision, Resources, Project administration, Investigation, Funding acquisition, Conceptualization. **Takuro Daimaru:** Writing – review & editing, Writing – original draft, Visualization, Validation, Supervision, Software, Resources, Project administration, Methodology, Investigation, Funding acquisition, Formal analysis, Data curation, Conceptualization.

Declaration of competing interest

The authors declare that they have no known competing financial interests or personal relationships that could have appeared to influence the work reported in this paper.

Acknowledgments

This research was partly conducted at the Jet Propulsion Laboratory, California Institute of Technology, USA, under internal research and technology development funding. In addition, this research was partly supported through computational resources and services provided by Advanced Research Computing at the University of Michigan, Ann Arbor. Finally, this material is based upon work supported by the National Science Foundation Graduate Research Fellowship (L.F.), United States under Grant No. DGE2241144.

Appendix A. Supplementary materials

A. CFD validity studies: two-slug simulations and experiment comparison, mesh convergence, and multiphase models

B. Videos

(i) Peripheral distributions of the liquid velocity vector and liquid volume fraction, in square channel. $u_{g,i} = 0.5$ m/s, R-134a, and $W = 1$ mm.

(ii) Distributions of the liquid volume fraction α_l, phase change rate, and temperature, in square channel. $q = 0.703$ W/cm^2, $u_{g,i} = 0.5$ m/s, R-134a, and $W = 1$ mm.

(iii) Peripheral distributions of the liquid volume of fraction and evaporation rate, in square channel. $q = 0.703$ W/cm^2, $u_{g,i} = 0.5$ m/s, R-134a, and $W = 1$ mm.

Supplementary material related to this article can be found online at https://doi.org/10.1016/j.ijheatmasstransfer.2025.126711.

Data availability

Data will be made available on request.

References

[1] A. Facin, L. Betancur, M. Mantelli, J.P. Florez, B. Coutinho, Influence of channel geometry on diffusion bonded flat plate pulsating heat pipes, in: Joint 19th IHPC and 13th IHPS, 2018.
[2] O. Ibrahim, J.G. Monroe, S.M. Thompson, N. Shamsaei, H. Bilheux, A. Elwany, L. Bian, An investigation of a multi-layered oscillating heat pipe additively manufactured from Ti-6Al-4V powder, Int. J. Heat Mass Transfer 108 (2017) 1036–1047.
[3] H.Y. Noh, A. Yoon, S.J. Kim, Investigation into the effect of transverse conduction on the thermal performance of a flat-plate pulsating heat pipe, Int. J. Heat Mass Transfer 181 (2021) 121842.
[4] S. Khandekar, Thermofluid dynamic study of flat-plate closed loop pulsating heat pipes, Microscale Thermophys. Eng. (2010).
[5] M. Magnini, O. Matar, Morphology of long gas bubbles propagating in square capillaries, Int. J. Multiph. Flow 129 (2020) 103353.
[6] S. Son, L. Chen, Q. Kang, D. Derome, J. Carmeliet, Contact angle effects on pore and corner arc menisci in polygonal capillary tubes studied with the pseudopotential multiphase lattice Boltzmann model, Computation 4 (2016) 12.
[7] F. Chauvet, P. Duru, M. Prat, Depinning of evaporating liquid films in square capillary tubes: Influence of corners' roundedness, Phys. Fluids 22 (2010) 112113.
[8] S. Jun, S. Kim, Comparison of the thermal performances and flow characteristics between closed-loop and closed-end micro pulsating heat pipes, Int. J. Heat Mass Transfer 95 (2016) 890–901.
[9] K. Odagiri, K. Wolk, S. Cappucci, S. Morellina, S. Roberts, A. Pate, B. Furst, E. Sunada, T. Daimaru, Three-dimensional heat transfer analysis of flat-plate oscillating heat pipe, Appl. Therm. Eng. 195 (2021) 117189.
[10] Y. Han, N. Shikazono, Measurement of liquid film thickness in micro square channel, Int. J. Multiph. Flow 35 (2009) 896–903.
[11] A. Hazel, M. Heil, The steady propagation of a semi-infinite bubble into a tube of elliptical or rectangular cross-section, J. Fluid Mech. 470 (2002) 91–114.
[12] H. Wong, C. Radke, S. Morris, The motion of long bubbles in polygonal capillaries. Part 1. Thin films, J. Fluid Mech. 292 (1995) 71–94.
[13] H. Wong, C. Radke, S. Morris, The motion of long bubbles in polygonal capillaries. Part 2. Drag, fluid pressure and fluid flow, J. Fluid Mech. 292 (1995) 95–110.
[14] H. Chen, Z. Li, J. Li, Thin-film profile around long bubbles in square microchannels measured by chromatic interference method, Appl. Phys. Lett. 109 (2016) 041604.
[15] A. Ferrari, M. Magnini, J. Thome, Numerical analysis of slug flow boiling in square microchannels, Int. J. Heat Mass Transfer 123 (2018) 928–944.
[16] R. Gupta, D. Flectcher, B. Haynes, On the CFD modelling of Taylor flow in microchannels, Chem. Eng. Sci. 64 (2009) 2941–2950.
[17] J. Thome, V. Dupont, A. Jacob, Heat transfer model for evaporation in microchannels. Part I: presentation of the model, Int. J. Heat Mass Transfer 47 (2004) 3375–3385.
[18] V. Dupont, J. Thome, A. Jacob, Heat transfer model for evaporation in microchannels. Part II: comparison with the database, Int. J. Heat Mass Transfer 47 (2004) 3387–3401.
[19] Y. Yan, T. Lin, Evaporation heat transfer and pressure drop of refrigerant R-134a in a small pipe, Int. J. Heat Mass Transfer 41 (1998) 4183–4194.
[20] B. Agostini, Etude experimentale de l'ebullition de fluide refrigerant en convection force dans des mini-canaux (Ph.D. thesis), Universite Joseph Fourier, 2002.
[21] R. Cerbus, J. Sakakibara, G. Gioia, P. Chakraborty, The turbulent flow in a slug: a re-examination, J. Fluid Mech. 883 (2019) A13.
[22] S. Munir, M. Siddiqui, A. Aziz, M. Heikal, U. Farooq, Proper orthogonal decomposition based on vorticity: application in a two-phase slug flow, J. Fluid Eng. 144 (2022) 041501.
[23] R. Dreiling, V. Dubois, S. Zimmermann, T. Nguyen-Xuan, P. Schreivogel, F. di Mare, Numerical investigation of slug flow in pulsating heat pipes using an interface capturing approach, Int. J. Heat Mass Transfer 199 (2022) 123459.
[24] J. Jo, J. Kim, S.J. Kim, Experimental investigations of heat transfer mechanisms of a pulsating heat pipe, Energy Conersion Manag. 181 (2019) 331–341.
[25] M. Ando, A. Okamoto, H. Nagai, Effect of flow resistance of floating-type check valves on heat transfer characteristics of an oscillating heat pipe, ASME J. Heat Mass Tansfer 145 (2023) 101004.
[26] V.S. Nikolayev, Physical principles and state-of-the-art of modeling of the pulsating heat pipe: A review, Appl. Therm. Eng. 195 (2021) 117111.
[27] K. Muramatsu, Y. Youn, Y. Han, Y. Hasegawa, N. Shikazono, Numerical study on the effect of initial flow velocity on liquid film thickness of accelerated slug flow in a micro tube, Int. J. Heat Fluid Flow 54 (2015) 77–86.

[28] K. Krippner, T. Daimaru, M. Kaviany, A simple analytic, slug–deposited liquid film thermal resistance/conductance model for oscillating heat pipe, Int. J. Heat Mass Transfer 235 (2024) 126139.
[29] A. Yoon, H. Noh, S. Lee, S. Kim, Study on the effect of condenser configuration of pulsating heat pipes for space applications, Int. J. Therm. Sci. 208 (2025) 109418.
[30] R. Shah, A. London, Laminar Flow Forced Convection in Ducts, Acadamic Press, 1979.
[31] J. Brackbill, D. Kothe, C. Zemach, A continuum method for modeling surface tension, J. Comput. Phys. 100 (1992) 335–354.
[32] J. Lee, S. Kim, Effect of channel geometry on the operating limit of micro pulsating heat pipes, Int. J. Heat Mass Transfer 107 (2017) 204–212.
[33] W.D. Bascom, S.J. Kim, Studies with the blowing method of measuring liquid viscosity near a solid surface, J. Colloid Interface Sci. 66 (1978) 559–572.
[34] Y.J. Youn, K. Muramatsu, Y. Han, N. Shikazono, The effect of bubble deceleration on the liquid film thickness in microtubes, Int. J. Heat Fluid Flow 58 (2016) 84–92.
[35] T. Daimaru, H. Nagai, M. Ando, K. Tanaka, A. Okamoto, H. Sugita, Comparison between numerical simulation and on-orbit experiment of oscillating heat pipes, Int. J. Heat Mass Transfer 109 (2017) 791–806.
[36] L.M. Tam, A.J. Ghajar, Transitional heat transfer in plain horizontal tubes, Heat Transf. Eng. 27 (5) (2006) 23–38.
[37] S. Miesner, N. Bautista, K. Wolk, B. Furst, T. Daimaru, E. Sunada, S. Roberts, J. Bellardo, J. Kuo, An experimental investigation of the relationship between evaporator and condenser sizes with oscillating heat pipe start-up, in: International Mechanical Engineering Congress and Exposition, IMECE, 2023.
[38] O. Castro, K. Wolk, B. Furst, E. Sunada, S. Roberts, T. Daimaru, J. Kuo, J. Bellardo, Experimental investigation of evaporator and condenser placement configuration for oscillating heat pipes, in: International Mechanical Engineering Congress and Exposition, IMECE, 2022.
[39] W. Kim, S.J. Kim, Fundamental issues and technical problems about pulsating heat pipes, ASME J. Heat Transf. 143 (2021) 100803–1.
[40] T. Daimaru, H. Nagai, M. Ando, K. Tanaka, A. Okamoto, H. Sugita, Comparison between numerical simulation and on orbit experiment of oscillating heat pipes, in: 46th International Conference on Environmental Systems, 2016.
[41] H.Y. Noh, S.J. Kim, Numerical simulation of pulsating heat pipes: Parametric investigation and thermal optimization, Energy Convers. Manage. 203 (2020) 1112237.
[42] V. Ayel, L. Araneo, A. Scalambra, M. Mameli, C. Romestant, A. Piteau, M. Marengo, S. Filippeschi, Y. Bertin, Experimental study of a closed loop flat plate pulsating heat pipe under a varying gravity force, Int. J. Therm. Sci. 96 (2015) 23–34.